

The impact of atmospheric motions on source-specific black carbon and the induced direct radiative effects over a river-valley region

Huikun Liu¹, Qiyuan Wang^{1,2,4*}, Suixin Liu^{1,5}, Bianhong Zhou³, Yao Qu¹, Jie Tian¹, Ting Zhang¹, Yongming Han^{1,2,4}, Junji Cao^{6,5*}

¹Key Laboratory of Aerosol Chemistry and Physics, State Key Laboratory of Loess and Quaternary Geology, Institute of Earth Environment, Chinese Academy of Sciences, Xi'an, 710061, China

²CAS Center for Excellence in Quaternary Science and Global Change, Xi'an, 710061, China

³Shaanxi Key Laboratory of Disaster Monitoring and Mechanism Simulation, College of Geography & Environment, Baoji University of Arts & Sciences, Baoji 721013, China

⁴Guanzhong Plain Ecological Environment Change and Comprehensive Treatment National Observation and Research Station, Xi'an 710061, China

⁵Shaanxi Key Laboratory of Atmospheric and Haze-fog Pollution Prevention, Xi'an 710061, China

⁶Institute of Atmospheric Physics, Chinese Academy of Sciences, Beijing 100029, China

*Correspondence to: Qiyuan Wang (wangqy@ieecas.cn) and Junji Cao (jjcao@mail.iap.ac.cn)

Abstract. Black carbon (BC) is one of the most important short lived climate forcers, and atmospheric motions play an important role in determining its mass concentrations of pollutants. Here an intensive observation was launched in a typical river-valley city to investigate relationships between atmospheric motions and BC aerosols. Equivalent BC (eBC) source apportionment was based on an aethalometer model with the site-dependent absorption Ångström exponents (AAEs) and the mass absorption cross-sections (MACs) retrieved using a positive matrix factorization (PMF) model based on observed chemical components (i.e. EC, POC, K⁺, Mg, Al, Si, S, Cl, Ca, V, Mn, Fe, Ni, Cu, As, Se, Br, Sr, Pb, Ga, and Zn) and primary absorption coefficients at selected wavelengths from $\lambda = 370$ to 880nm. The derived AAEs from 370 to 880nm were 1.07 for diesel vehicular emissions, 2.13 for biomass burning, 1.74 for coal combustion, and 1.78 for mineral dust. The mean values for eBC_{fossil} and eBC_{biomass} were 2.46 $\mu\text{g m}^{-3}$ and 1.17 $\mu\text{g m}^{-3}$ respectively. Wind run distances and the vector displacements of the wind in 24 h were used to construct a self-organizing map, from which four atmospheric motions categories were identified (local-scale dominant, local-scale strong and regional-scale weak, local-scale weak and regional-scale strong and regional-scale dominant). BC pollution was found to be more likely when the influence of local-scale motions outweighed those of regional-scale motions. Cluster analysis for the back trajectories of air mass calculated by Hybrid Single-Particle Lagrangian Integrated Trajectory model at the study site indicated that the directions of air flow can have different impacts for different scales of motion. The direct radiative effects (DRE) of source-specific eBCs were lower when the influence of regional-scale motions outweighed that of the local ones. However, due to chemical aging of the particles during transport—the DRE efficiencies under regional scale motions were ~ 1.5 times higher than those under more local influences. The finding that the DRE efficiency of BC increased during the regional transport suggested significant consequences in regions downwind of pollution sources and emphasizes the importance of regionally transported BC for potential climatic effects.

36 **1 Introduction**

37 Black carbon (BC) is produced by the incomplete combustion of biomass and fossil fuels. The BC aerosol has a strong light
38 absorption capacity and can cause heating of the atmosphere. In fact, BC is widely recognized as one of the most important
39 short-lived climate forcers (IPCC, 2021). Due to this high light-absorbing ability, BC has the potential to perturb the radiative
40 balance between the earth and atmosphere and in so doing cause in the climate to change and drive ecosystems away from their
41 natural states (Schroter et al., 2005). Those changes ultimately will affect biodiversity and could threaten humans' food security
42 (Ochoa-Hueso et al., 2017; Shindell et al., 2012). Besides heating the atmosphere directly, BC also is important for nucleating
43 clouds, and that is another way in which the particles can cause indirect climatic effects (Jacobson, 2002). As BC is
44 heterogeneously distributed in the atmosphere, its climatic effects are highly variable and dependent on its distribution in the
45 atmosphere, both horizontally and vertically; its radiative properties and how they are affected by of chemical processing; and
46 its lifetime (IPCC, 2021).

47 The radiative efficiency of BC can vary due to differences in emission sources and atmospheric aging processes (Bond et al.,
48 2013; He et al., 2015; Cappa et al., 2012). Indeed, BC from different sources can vary in light absorbing abilities (Cheng et al.,
49 2011) which can affect the radiative forcing of climate. In addition to the effects of the sources, regional transport can impact
50 the light-absorbing ability through chemical processing or aging (Zhang et al., 2019). After BC particles are emitted, they can
51 stay in the atmosphere for days or a few weeks (IPCC, 2021). During transport, fresh BC can experience a series of physical
52 and chemical changes, for instance, mixing with other substances that can alter its microphysical and optical properties (Kahnert
53 and Kanngießer, 2020). The aging processes can be even faster in polluted regions (Peng et al., 2016), and as a result, the light-
54 absorbing ability of BC can be strongly affected. Indeed, the light absorption ability of BC after aging can be as much as 2.4
55 times that of fresh particles (Peng et al., 2016).

56 The concentrations of BC are controlled by local emissions and regional transport, but meteorological conditions also are
57 important because they affect both transport and removal. Normally, local emissions in urban areas are predictable to some
58 degree because those emission sources are mainly anthropogenic and the concentrations of pollutants follow the diurnal patterns
59 driven by anthropogenic activities. By contrast, meteorological conditions and regional transport are governed by multiple
60 scales of motion which result in distinct meteorological impacts on ambient pollutant levels (Levy et al., 2010, Dutton, 1976).
61 A commonly accepted classification of the scale of motion is based on horizontal distance and time scales. Typically, the time
62 scale of local-scale motions varies from hours to days and the spatial scale ranges from 10^2 to 10^5 m (Oke et al., 2002; Seinfeld
63 and Pandis, 2006). The local scales of motion are mainly controlled by local factors such as the roughness of the earth's surface,
64 orography, land breeze/sea breeze circulation, etc. (Hewitson and Crane, 2006; IPCC, 2021). Larger scale of motions are
65 associated with a mesoscale or synoptic scale weather systems, which on the one hand can transport pollutants but on the other
66 can disperse them (Kalthoff et al., 2000; Zhang et al., 2012).

67 The relationships between atmospheric motions and pollutant concentrations are complex. Atmospheric motions determine
68 where and how extensive the pollution impacts are, but of course the rates of pollutant emissions, especially local ones, are
69 important, too (Dutton, 1976). Liao et al., (2020) found that synoptic-scale flow led to an enhanced $PM_{2.5}$ in a coastal area of
70 the Pearl River Delta, while meso/local scale motions led to $PM_{2.5}$ pollution in an inland area. Levy et al. (2010) showed that
71 the concentrations of NO_x and SO_2 were higher under the dominance of smaller-scale motions than under larger scale motions.

72 However, few studies have touched on the impacts of different scales of motion on BC and their effects on radiative efficiency
73 even though the effects could cause rapid climatic effects due to the patchy and constantly changing distributions (IPCC, 2021).
74 Topography also plays an important role in air pollution (Zhao et al., 2015). River-valley topography is complicated, and it can
75 have a considerable influence on air pollution and synoptic patterns of flow (Green et al., 2016; Carvalho et al., 2006). The
76 pollution levels at cities in river-valleys are not only influenced by general atmospheric dynamics but also strongly impacted
77 by the local-scale of dynamics (Brulfert et al., 2006). Surface albedo and surface roughness are affected by the complex
78 topography of river-valley regions, and those physical factors can affect circulation causing changes in pollutant mass
79 concentrations (Wei et al., 2020). Mountains also significantly affect pollution, and once pollutants are generated or transported
80 into the river-valley regions, their dispersal can be impeded by the blocking effect of the mountains. Instead of being dispersed,
81 they can be carried by the airflows over the mountains to converge at the bottom of the valley and increase the pollutants along
82 the river (Zhao et al., 2015). In this way, pollutants can accumulate in valleys and spread throughout the area, thereby
83 aggravating pollution. In addition, temperature inversions commonly form in river-valleys during the winter, and that, too, can
84 aggravate pollution problems (Glojek et al., 2022 and Bei et al., 2016).
85 Thus, we focused our study on the impacts of different scales of motion on source-specific equivalent BCs (eBCs), and we
86 evaluated radiative effects of eBCs over a river-valley city. The primary objectives of this study were: (1) to quantify the
87 contributions of fossil fuel combustion and biomass burning to eBC concentrations, (2) to investigate the impacts of different
88 scales of motion on the source-specific eBC, and (3) to estimate the radiative effects and the radiative efficiency of the source-
89 specific eBC under different atmospheric motion scenarios. The study provides insights into the influence of the specified
90 atmospheric motions on BC and highlights the effects of those motions on the radiative efficiency and potential climatic effects
91 of the regionally transported BC.

92 **2 Methodology**

93 **2.1 Research site**

94 Baoji is a typical river-valley city, located at the furthest west of the Guanzhong Plain, at an altitude from 450 to 800 m a.s.l.
95 (Figure S1), Baoji has a complex topography and often suffering from severe pollution in winter. It is surrounded by mountains
96 to the south, west and north, with the Weihe River as the central axis extending eastward. The shape can be viewed as a funnel,
97 with large opening to east. The Qinling peaks and the flat Weihe Plain are the main landforms of Baoji. The main peak of the
98 Qinling Mountains is 3,767 m a.s.l. and it is the highest mountain in the eastern part of mainland China. This terrain causes
99 divergent flow at local scales, which can impact pollution levels (Wei et al., 2020). Baoji also is an important railway
100 intersection in China, connecting six railways to the north-west and southwest China. Pollutant levels can be high and pollutants
101 are not easy to be dispersed in the city due to its special topographic conditions, dense population (total population of 0.341
102 million, with 63.5% population living in the downtown area and population density of 6003 people per km² in 2019
103 (<http://tjj.shaanxi.gov.cn/upload/2021/zk/indexch.htm> and <https://data.chinabaogao.com/hgshj/2021/042053X932021.html>),
104 and impacts from major highway and railway networks.

105 The sampling site was on the rooftop of a building at Baoji University of Arts and Sciences (34°21'16.8"N, 107°12'59.6"E,
106 569 m a.s.l.) surrounded by commercial and residential buildings, highways, and a river, there were no major industrial emission
107 sources nearby. The main sources of BC in Baoji were the domestic fuel (coal and biomass) burning as well as the motor
108 vehicle emissions (Zhou et al., 2018; Xiao et al., 2014). Open fire also can be sources for BC, but there were limited fire found
109 scattered around the site (Figure S2). The meteorological conditions at Baoji for the four seasons are listed in Table S1, and the
110 wind roses for the different seasons are shown in Figure S3(data are from the Meteorological Institute of Shaanxi Province).

111 2.2 Sampling and laboratory measurements

112 eBC and the absorption coefficients (b_{abs}) at 370, 470, 520, 590, 660, 880, and 950 nm wavelength were measured using an
113 AE33 aethalometer (Magee Scientific, Berkeley, CA, USA) equipped with a PM_{2.5} cut-off inlet (SCC 1.829, BGI Inc. USA)
114 that had a time resolution of 1 min. A Nafion® dryer (MD-700-24S-3; Perma Pure, Inc., Lakewood, NJ, USA) with a flow rate
115 of 5 L min⁻¹ was used to dry the PM_{2.5} before the measurement. Briefly, the particles were dried by the Nafion® dryer before
116 being measured with the AE33 aethalometer, and the deposited particles were irradiated by light-emitting diodes at seven
117 wavelengths of light-emitting diodes ($\lambda = 370, 470, 520, 590, 660, 880, \text{ and } 950 \text{ nm}$), and the light attenuation was detected.
118 The non-linear loading issue for filter-based absorption measurement was accounted for in the AE33 by a technique called
119 dual-spot compensation. The quartz filter (PN8060) matrix scattering effect was corrected by using a factor of 1.39. More
120 details of AE33 measurement techniques can be found in Drinovec et al. (2015).

121 The scattering coefficient (b_{scat}) at a single (525) nm wavelength was measured with the use of a nephelometer (Aurora-1000,
122 Ecotech, USA) that had a time resolution of 5 min. The nephelometer and aethalometer operated simultaneously and used the
123 same PM_{2.5} cyclone and Nafion® dryer. The calibration was conducted based on the user guide with a calibration gas R-134.
124 Zero calibrations were conducted every other day by using clean air without particles. The ambient air was drawn in through a
125 heated inlet with a flow rate of 5 L min⁻¹. The relative humidity remained lower than 60%.

126 PM_{2.5} samples were collected for every 24 hours (h) from 10 a.m. local time to the 10 a.m. the next day from 16th November
127 2018 to 21st December 2018 with two sets of mini-volume samplers (Airmetrics, USA), one using quartz fiber filters (QM/A;
128 Whatman, Middlesex, UK) and the other with Teflon® filters (Pall Corporation, USA), both with a flow rate of 5 L min⁻¹.
129 Those samples were kept in a refrigerator at 4°C before analysis. The mass concentration of K⁺ in the PM_{2.5} quartz sample was
130 extracted in a separate 15 mL vials containing 10 mL distilled deionized water (18.2 MΩ resistivity). The vials were placed in
131 an ultrasonic water bath and shaken with a mechanical shaker for 1 h to extract the ions and determined by a Metrohm 940
132 Professional IC Vario (Metrohm AG., Herisau, Switzerland) with Metrosep C6-150/4.0 column (1.7 mmol/L nitric acid+1.7
133 mmol/L dipicolinic acid as the eluent) for cation analysis. A group of elements (i.e. Mg, Al, Si, S, Cl, Ca, V, Mn, Fe, Ni, Cu,
134 As, Se, Br, Sr, Pb, Ga, and Zn) on the Teflon® filters was determined by energy-dispersive x-ray fluorescence (ED-XRF)
135 spectrometry (Epsilon 4 ED-XRF, PANalytical B.V., Netherlands). The X-rays were generated from a gadolinium anode on a
136 side-window X-ray tube. A spectrum of the ratio of X-ray and photon energy was obtained after 24 minutes of analysis for
137 each sample with each energy peak characteristic of a specific element, and the peak areas were proportional to the
138 concentrations of the elements. Quality control was conducted on a daily basis with test standard sample.

139 Organic carbon (OC) and elemental carbon (EC) in each sample were determined with the use of a DRI Model 2001
140 Thermal/Optical Carbon Analyzer (Atmoslytic Inc., Calabasas, CA, USA). The thermal/optical reflectance (TOR) method and
141 IMPROVE_A protocol were used for analysis. A punch of a quartz filter sample was heated at specific temperatures to obtain
142 data for four OC fractions and three EC fractions. Total OC was calculated by summing all OC fractions and the pyrolyzed
143 carbon (OP) produced. Total EC was calculated by summing all EC fractions minus the OP. Detailed methods and quality
144 assurance/quality control processes were described in Cao et al., (2003). Primary organic carbon (POC) was estimated by using
145 the minimum R-squared (MRS) method, which is based on using eBC as a tracer (Text S1). The method uses the minimum R²
146 between OC and eBC to indicate where the ratio for which secondary OC and eBC are independent. A detailed description of
147 the MRS method can be found in Wu et al., (2016).

148 Data for NO_x, wind speed, and direction at 12 ground monitoring sites were downloaded from
149 http://sthjt.shaanxi.gov.cn/hx_html/zdjkqy/index.html. The wind data at 100 meters (m) above the ground and the planetary
150 boundary layer height were downloaded from <https://rda.ucar.edu/datasets/ds633.0>. The data used for the Hybrid Single-
151 Particle Lagrangian Integrated Trajectory (HYSPPLIT) model was downloaded from Global Data Assimilation System
152 and it had a resolution of 1°×1° (GDAS, <https://www.ready.noaa.gov/gdas1.php>). The data and main parameters used in
153 trajectory model are listed in Table S2.

154 2.3 Optical source apportionment

155 The positive matrix factorization (PMF) model that was used for the optical source apportionment in this study. PMF solves
156 chemical mass balance by decomposing the observational data into different source profiles and contribution matrices as
157 follows:

$$158 X_{ij} = \sum_{k=1}^p g_{ik}f_{kj} + e_{ij} \quad (1)$$

159 where X_{ij} denotes the input data matrix; p is the number of sources selected in the model; g_{ik} denotes the contribution of the
160 k^{th} factor to the i^{th} input data; f_{kj} represents the k^{th} factor's profile of the j^{th} species; and e_{ij} represents the residual. Both g_{ik} and
161 f_{kj} are non-negative. The uncertainties of each species and $b_{\text{abs}}(\lambda)$ were calculated by the equation recommended in EPA
162 PMF5.0 user guideline(Norris et al, 2014) as follows:

$$163 \text{Unc} = \sqrt{(\text{error fraction} \times \text{concentration}(\text{or lighth absorption coefficient}))^2 + (0.5 \times \text{MDL})^2} \quad (2)$$

$$164 \text{Unc} = \frac{5}{6} \times \text{MDL} \quad (3)$$

165 where MDL is the minimum detection limit of the method. When the concentration of a species was higher than the MDL then
166 equation (2) was used otherwise equation (3) was used. In equation (2), for calculating the uncertainty of a chemical species,
167 the error fraction was multiplied the concentration of the species. For calculating the uncertainty of optical data, the error
168 fractions were multiplied by the light absorption coefficients.

169 Chemical species data (EC, POC, K⁺, Mg, Al, Si, S, Cl, Ca, V, Mn, Fe, Ni, Cu, As, Se, Br, Sr, Pb, Ga and Zn) and the primary
170 absorption coefficients (Pabs) data at $\lambda=370\text{nm}, 470\text{nm}, 520\text{nm}, 660\text{nm}$, and 880nm were used for PMF analysis. The error
171 fraction of offline measured data was the difference between multiple measurements of the same sample. The error fraction

172 used for optical data was 10% based on Rajesh and Ramachandran (2018). PMF solves the equation (1) by minimizing the Q
 173 value, which is the sum of the normalized residuals' squares, as follows,

$$174 \quad Q = \sum_{i=1}^n \sum_{j=0}^n \left[\frac{e_{ij}}{u_{ij}} \right]^2 \quad (4)$$

175 where u_{ij} represents the uncertainties of each X_{ij} and $Q_{\text{true}}/Q_{\text{exp}}$ was used as the indicators for the factor number determination.

176 2.4 eBC source apportionment

177 The quantities of eBC generated from biomass burning versus fossil fuel combustion were deconvolved by an aethalometer
 178 model which uses Beer-Lambert's Law to write the absorption coefficients equations, wavelengths and absorption Ångström
 179 exponents (AAEs) for the two different BC emission sources (Sandradewi et. al., 2008). This approach is widely used for
 180 separating BC from two different sources based on optical data (Rajesh et al., 2018; Kant et al., 2019; Panicker et al., 2010).
 181 However, the traditional aethalometer model could be affected by the light absorbing substances at lower wavelengths such as
 182 dust and secondary formation particles. An improvement to the traditional aethalometer model was made, by explicitly
 183 considering the interference of the b_{abs} at a lower wavelength (370nm) caused by dust and secondary OC. Thus, the calculation
 184 of the absorption and source apportionment was based on the following equations (Wang et al., 2020):

$$185 \quad \frac{b_{\text{abs}}(370)_{\text{fossil}}}{b_{\text{abs}}(880)_{\text{fossil}}} = \left(\frac{370}{880} \right)^{-AAE_{\text{fossil}}} \quad (5)$$

$$186 \quad \frac{b_{\text{abs}}(370)_{\text{biomass}}}{b_{\text{abs}}(880)_{\text{biomass}}} = \left(\frac{370}{880} \right)^{-AAE_{\text{biomass}}} \quad (6)$$

$$187 \quad b_{\text{abs}}(880) = b_{\text{abs}}(880)_{\text{fossil}} + b_{\text{abs}}(880)_{\text{biomass}} \quad (7)$$

$$188 \quad b_{\text{abs}}(370) = b_{\text{abs}}(370)_{\text{fossil}} + b_{\text{abs}}(370)_{\text{biomass}} + b_{\text{abs}}(370)_{\text{secondary}} + b_{\text{abs}}(370)_{\text{dust}} \quad (8)$$

$$189 \quad eBC_{\text{fossil}} = \frac{b_{\text{abs}}(880)_{\text{fossil}}}{MAC_{BC}(880)_{\text{fossil}}} \quad (9)$$

$$190 \quad eBC_{\text{biomass}} = \frac{b_{\text{abs}}(880)_{\text{biomass}}}{MAC_{BC}(880)_{\text{biomass}}} \quad (10)$$

191 where AAE_{fossil} and AAE_{biomass} are the AAEs for fossil fuel combustion and biomass burning. These were derived from the
 192 optical source apportionment by using PMF as discussed in section 3.1. Further, $b_{\text{abs}}(370)$ and $b_{\text{abs}}(880)$ are the total b_{abs}
 193 measured by the AE33 at the wavelengths of 370 nm and 880 nm respectively; $b_{\text{abs}}(370)_{\text{fossil}}$ and $b_{\text{abs}}(880)_{\text{fossil}}$ are the b_{abs} caused
 194 by emissions from fossil fuel combustion at those two wavelengths; $b_{\text{abs}}(370)_{\text{biomass}}$ and $b_{\text{abs}}(880)_{\text{biomass}}$ are the b_{abs} caused by
 195 emissions from biomass burning at those two wavelengths; $b_{\text{abs}}(370)_{\text{dust}}$ refers to the b_{abs} contributed by mineral dust at the
 196 wavelength of 370 nm, which was derived from the result of optical source apportionment; $b_{\text{abs}}(370)_{\text{secondary}}$ refers to the b_{abs}
 197 caused by the secondary aerosols at the wavelength of 370 nm, which was calculated by the minimum R -squared approach with
 198 eBC as a tracer (Text S1, Wang et al., 2019); eBC_{fossil} and eBC_{biomass} are the eBCs from fossil fuel combustion and biomass
 199 burning; and $MAC_{BC}(880)_{\text{fossil}}$ and $MAC_{BC}(880)_{\text{biomass}}$ are the mass absorption cross-sections of eBC_{fossil} and the mass
 200 absorption cross-section of eBC_{biomass} at the wavelength of 880 nm respectively, which were based on the PMF results for the
 201 optical source apportionments.

202 2.5 Indicators for the different scales of motion

203 The mathematical definitions of airflow condition proposed by Allwine and Whiteman (1994) were used in this study. The
204 definitions quantify the flow features integrally at individual stations. Three variables were quantified, namely the actual wind
205 run distance (S) which is the scalar displacement of the wind in 24 h (i.e. the accumulated distance of the wind), the resultant
206 transport distance (L) which is the vector displacement of the wind in 24 h (i.e. the straight line from the starting point to the
207 end point), and the recirculation factor (R) is based on the ratio of L and S which indicates the frequency of the wind veering
208 in 24 h. The influences of different scales of atmospheric motions were assessed based on the method proposed by Levy et al.,
209 (2010), and for this, we used wind data at 100 m above the sampling site and the wind data from 12 monitoring stations at
210 ground level (~15m) to indicate the different scales of motions. The winds at the surface monitoring stations were expected to
211 be more sensitive to local-scale turbulence and convection than the winds at 100 m. With less influence from the surface forces,
212 the indicators at 100 m would be more sensitive to larger scales of motion. The equations used as follows:

$$213 L_{n\tau/bj} = T \left[\left(\sum_{j=i}^{i-\tau+1} u_i \right)^2 + \left(\sum_{j=i}^{i-\tau+1} v_i \right)^2 \right]^{1/2} \quad (11)$$

$$214 S_{n\tau/bj} = \sum_{j=i}^{i-\tau+1} (u_j^2 + v_j^2)^{1/2} \quad (12)$$

$$215 R_{n\tau/bj} = 1 - \frac{L_{i\tau}}{S_{i\tau}} \quad (13)$$

216 where T is the interval of the data (i.e., 60 min), i is the i^{th} the ending time step data, τ is the integration time period of the wind
217 run (24 h), $i-\tau+1$ represents the data at the start time, and n is the number of monitoring stations (a total of 12 in this study).
218 The quantities u and v are the wind vectors. Using the wind data from the 12 monitoring stations covering Baoji, the L and S
219 values at the 12 different sites at ground level were calculated. $L_{n\tau}$ and $S_{n\tau}$ represent the resultant transport distance and the
220 actual wind run distance at the n^{th} ($n = 1$ to 12) monitoring station at ground level; $R_{n\tau}$ is the recirculation factor at the n^{th}
221 monitoring station which is calculated based on $L_{n\tau}$ and $S_{n\tau}$; L_{bj} and S_{bj} are the resultant transport distance and the actual wind
222 run distance at 100 m height above the ground. These represent the flow characteristics in higher atmosphere at the study site,
223 and they were calculated by using the wind data at 100 m height. The recirculation factor (R_{bj}) was calculated for a height of
224 100 m.

225 As explained in Levy et al., (2010), if local-scale motions are strong and regional-scale motions are weak, the variations in
226 winds at each station would not be likely to be uniform due to differences in local factors, and that would result in relatively
227 large standard deviations (R_{std}) for $R_{n\tau}$. By contrast, if the local-scale motions are weak and the regional-scale motions are
228 strong, the wind direction would be likely to be more uniform over a large area, and the R_{bj} and the R_{std} should be relatively
229 smaller.

230 2.6 Self-organizing map

231 A self-organizing map (SOM) developed by Kohonen (1990) is a type of artificial neural network that is widely used for
232 categorizing high-dimensional data into a few major features (Stauffer et al., 2016 and Pearce et al., 2014). In particular, this
233 approach is widely used for categorizing different meteorological patterns (Liao et al., 2020; Han et al., 2020; Jiang et al.,
234 2017). Unlike traditional dimension reduction methods (e.g., principal component analysis), SOM projects high-dimensional

235 input data by non-linear projection into user-designed lower-dimensions, which are typically two-dimensional arrays of nodes
 236 (Hewitson and Crane, 2006). The performance of SOM in classifying climatological data has been shown to be robust (Reusch
 237 et al., 2005). Competitive learning algorithms are used to train SOM, and the architecture of SOM consists of two layers; one
 238 is called the input layer and it contains the high dimensional input data. The other layer is the output layer in which the node
 239 number is the output cluster number. The working principle of SOM is to convert high dimensional data with complex
 240 correlations into lower dimensions via geometrical relationships (Ramachandran et al., 2019). After the initial random weights
 241 are generated, the input data are compared with each weight, and the best match is defined as winning. The winning node and
 242 the neighboring nodes close to the winning node will learn from the same inputs and the associated weights are updated. After
 243 multiple iterations, the network settles into stable zones of features and the weights. More detailed working principles of
 244 SOM can be found Kangas and Kohonen, (1996) and Kohonen et al., (1996).

245 Comparison between the input data and each weight is made by applying Euclidean distances, the best match is defined by the
 246 following equation:

$$247 \quad \|x - m_c\| = \min\{\|x - m_i\|\} \quad (14)$$

248 where x is the input data, m_c is the best matched weight, m_i is the weights connected with the i^{th} node.

249 The weights are updated by following equation:

$$250 \quad m_i(t + 1) = m_i(t) + h_{ci}(t)[x(t) - m_i(t)] \quad (15)$$

251 where the $m_i(t + 1)$ is the i^{th} weight at $t+1$ time, $m_i(t)$ is the i^{th} weight at t time, the $h_{ci}(t)$ is the neighborhood kernel defined
 252 over the lattice points at t time, and c is the winning node location.

253 SOM was used to categorize the daily atmospheric motions during the study period and to explore the influences of different
 254 scales of motion on source-specific eBC. Hourly averages of three sets of data (R_{std} , L_{bj} , and S_{bj}) were input into SOM.
 255 Determining the size of the output map is crucial for SOM (Chang et al 2020 and Liu et al., 2021). To reduce the subjectivity,
 256 the K-means cluster method was used for the decision-making regarding size. The similarity of each item of the input data
 257 relative to the node was measured using Euclidean distance. The iteration number was set to 2000. For each input data item,
 258 the node closest to it would “win out”. The reference vectors of the winning node and their neighborhood nodes were updated
 259 and adjusted towards the data. The “Kohonen” package in *R* language (Wehrens and Kruisselbrink, 2019) was used to develop
 260 the SOM model in this study.

261 **2.7 Estimations of direct radiative effects and heating rate**

262 The Santa Barbara DISORT Atmospheric Radiative Transfer (SBDART) model was used to estimate the direct radiative effects
 263 (DRE) induced by source-specific eBC. The model has been used in many studies to calculate the DRE caused by aerosols and
 264 BC (Pathak et al., 2010; Rajesh et al., 2018; Zhao et al., 2019). SBDART calculated DRE based on several well-tested physical
 265 models. Details regarding the model were presented in Ricchiazzi et al., (1998). The important input data included aerosol

266 parameters, including aerosol optical depth (AOD), single scattering albedo (SSA), asymmetric factor (AF) and extinction
267 efficiency, surface albedo, and atmospheric profile.

268 The aerosol parameters used in this study were derived by the Optical Property of Aerosol and Cloud (OPAC) model (Hess et
269 al., 1998) based on the number concentrations of aerosol components. As the study was conducted in an urban region, the urban
270 aerosol profile was used in OPAC, and it included soot (eBC), water-soluble matter (WS), and water-insoluble matter (WIS).
271 The number concentrations of soot were derived from the mass concentrations of eBC with the default ratio ($5.99E-5 \mu\text{g m}^{-3}/$
272 particle.cm^{-3}) in OPAC. The number concentrations of WS and WIS were adjusted until the modeled SSA and b_{abs} at 500nm
273 in OPAC were close ($\pm 5\%$, see Figure S4) to those values calculated with data from the nephelometer and AE33 ($b_{\text{ext}}(520) =$
274 $b_{\text{scat}}(525) + b_{\text{abs}}(520)$, $\text{SSA} = b_{\text{scat}}(525)/b_{\text{ext}}(520)$). The DRE of source-specific eBC at the top of atmosphere (TOA) and surface
275 atmosphere (SUF) were calculated from the difference between the DREs with or without the number concentrations of the
276 source-specific eBC under clear-sky conditions.

$$277 \quad DRE_{eBC} = (F \downarrow - F \uparrow)_{\text{with } eBC} - (F \downarrow - F \uparrow)_{\text{without } eBC} \quad (16)$$

$$278 \quad DRE_{eBC,ATM} = DRE_{eBC,TOA} - DRE_{eBC,SUF} \quad (17)$$

279 where DRE_{eBC} is the DRE of source-specific eBC, $F \downarrow$ and $F \uparrow$ are the downward and upward flux, $DRE_{eBC,ATM}$ is the DRE of
280 the source-specific eBC for the atmospheric column, that is, the DRE at the top of the atmosphere ($DRE_{eBC,TOA}$) minus that at
281 the surface ($DRE_{eBC,SUF}$).

282 **3 Results and discussion**

283 **3.1 Calculation of eBC_{fossil} and eBC_{biomass}**

284 The PMF model was used for the optical source apportionment, and those results were used to obtain the site-specific AAEs
285 and MACs, which in turn were used to calculate the source-specific eBC with the improved aethalometer model. For every
286 solution, PMF was run 20 times. The $Q_{\text{true}}/Q_{\text{exp}}$ ratios from the 2- to 7-factor solutions were examined, and the values of a 4-
287 factor solution were found most stable compared with others because the $Q_{\text{true}}/Q_{\text{exp}}$ values did not drop appreciably after the
288 addition of one more factor (Figure S5). Based on these results, the 4-factors solution was determined to be the most
289 interpretable. Two diagnostic methods, Bootstrap (BS) and Displacement (DISP) (Norris et al, 2014; Brown et al. 2015) were
290 used to validate the robustness and stability of the results. The BS method was used to assess the random errors and partially
291 assess the effects of rotational ambiguity while DISP was used to evaluate rotational ambiguity errors. The results of the BS
292 and DISP analyses showed that there was no swap for the 4-factor solution (Table S3). The modelled primary $b_{\text{abs}}(\lambda)$ were well
293 correlated ($r = 0.95-0.96$, slope = $0.90-0.95$, $p < 0.01$, Figure S6) with their observed counterparts, which suggested that the
294 modelling performance of PMF5.0 was good. The factor profiles obtained from the PMF are shown in Figure 1.

295 The first factor (PC1) had was featured with high loadings of EC (52%), POC (49%), and V (49%) and moderate loadings of
296 Mn (33%), Ni (40%), Cu (37%), and Zn (44%). This factor source contributed 27% to 44% of the primary $b_{\text{abs}}(\lambda)$. Of the species
297 with high loadings on PC1, EC has been found to be associated with vehicular emissions due to incomplete fuel combustion
298 (Cao et al., 2013). V and Ni are commonly detected in the particles emitted by diesel-powered vehicles (Lin et al., 2015 and

299 Zhao et al., 2021). Mn compounds are commonly used as an antiknock additive for unleaded gasoline to raise octane numbers
300 and protect the engine (Lewis et al., 2003; Geivanidis et al., 2003); and Cu and Zn are emitted by the combustion of lubricating
301 oils and from the wear of motor vehicle parts (i.e., brakes and tires) (Thorpe and Harrison, 2008; Song et al., 2006). In addition,
302 the EC associated with this factor was found well correlated ($r = 0.83$, $p < 0.01$, Figure S7) with the daily averaged NO_x which
303 is a commonly used tracer of vehicular emissions in the urban areas (Zotter et al., 2017). Recent research on the source
304 contributions of BC emissions has shown that most of BC associated with transportation was emitted by on-road diesel vehicles
305 in China (Xu et al., 2021). From these results, PC1 was identified as diesel vehicular emissions. The MAC of this factor (MAC
306 $(880)_{\text{diesel}}$) was $6.7 \text{ m}^2 \text{ g}^{-1}$. The estimated AAE of this factor (AAE_{diesel}) was 1.07 (Figure S8), which is comparable with the
307 AAE values of vehicle emissions (0.8~1.1) reported in previous studies (Zotter et al., 2017; Kirchstetter et al., 2004).

308 The second factor (PC2) was characterized by the high loadings of K^+ (51%), Cl (79%), and Br (52%) and moderate amounts
309 of EC (26%), POC (28%), and Pb (30%). Of these, K^+ is a widely recognized tracers for the biomass burning emissions (Urban
310 et al., 2012; Zhang et al., 2015), and high loadings of Cl also can be taken as a signal of biomass burning (Yao et al., 2002;
311 Manousakas et al., 2017). Previous studies showed that a large quantity of Br was found in biomass burning aerosols was
312 caused by emissions of CH_3Br emission during combustion (Manö and Andreae, 1994; Artaxo et al., 1998). Particulate matter
313 emitted from biomass burning typically has substantial amounts of OC and EC (Song et al., 2006), and Pb also has been observed
314 in biomass-burning aerosols (Amato et al., 2016). Thus, PC2 was identified as emissions from biomass burning. The
315 contribution of this factor to primary $b_{\text{abs}}(370)$ was as high as 50%, but only 33% to primary $b_{\text{abs}}(880)$, and that was likely
316 caused by the brown carbon which is a typically found in biomass-burning aerosols (Washenfelder et al., 2015; Yan et al.,
317 2015). The MAC of this factor (MAC $(880)_{\text{biomass}}$) was $9.5 \text{ m}^2 \text{ g}^{-1}$. The AAE of this factor (AAE_{biomass}) was 2.13 (Figure S8),
318 which is consistent with the wide range of AAEs reported for biomass-burning (1.2~3.5) (Sandradewi et al., 2008; Helin et al.,
319 2018; Zotter et al., 2017).

320 The third factor (PC3) had significant loadings of S (64%), Se (98%), As (51%), and Pb (53%) and moderate loadings of Ga
321 (42%)—all of these elements are commonly associated with coal combustion (Hsu et al., 2016; Tan et al., 2017). For instance,
322 coal combustion has gradually become the main source of Pb in $\text{PM}_{2.5}$ after China began to phase out Pb-containing gasoline
323 (Xu et al. 2012). Thus, PC3 was assigned to coal combustion. The MAC of this factor (MAC $(880)_{\text{coal}}$) was $7.5 \text{ m}^2 \text{ g}^{-1}$. This
324 factor contributed 17%–19% primary $b_{\text{abs}}(\lambda)$, and its derived AAE_{coal} was 1.74 (Figure S8) which is close to the AAE found for
325 coal-chunks (Sun et al., 2017).

326 The last factor (PC4) was most heavily loaded with Al (68%), Si (76%), Ca (65%), Fe (51%), and Sr (71%). These elements
327 are typical crustal elements, and they are abundant in mineral dust (Tao et al., 2016; Tao et al., 2017). Minor amounts of EC in
328 crustal dust could be from other EC that had deposited on the ground and later resuspended together with the dust by natural
329 or artificial disturbances (e.g., wind and traffic flow). This factor only contributed ~4% of the primary $b_{\text{abs}}(\lambda)$. The estimated
330 AAE_{dust} was 1.78 (Figure S8) which is close to the AAE of mineral dust reported in previous studies (AAE₃₇₀₋₉₅₀ = 1.82, Yang
331 et al., 2009).

332 As elaborated above, the $\text{PM}_{2.5}$ EC over Baoji was mainly from diesel vehicular emissions, biomass burning, and coal
333 combustion. The emissions can be further grouped into those from biomass burning and fossil fuel combustion (the sum of
334 diesel vehicular emissions and coal combustion). Thus, the AAE_{fossil} (1.26) and MAC $(880)_{\text{fossil}}$ ($7.1 \text{ m}^2 \text{ g}^{-1}$) were calculated

335 was the mass-weighted averages (relative to the total EC) of AAE_{coal} ($MAC(880)_{\text{coal}}$) and AAE_{diesel} ($MAC(880)_{\text{diesel}}$) (Table
336 S4). The hourly mass concentrations of eBC_{fossil} and eBC_{biomass} were then calculated using the ‘aethalometer model’ (Eqs. 5–
337 10). The results showed that eBC_{fossil} and eBC_{biomass} were only weakly correlated ($r = 0.3$, Figure S9), indicating a reasonably
338 good separation, and furthermore, their diel variations showed different patterns (Figure 2).

339 The mean values of eBC_{fossil} and eBC_{biomass} were $2.46 \mu\text{g m}^{-3}$ and $1.17 \mu\text{g m}^{-3}$, respectively. The averaged total eBC mass
340 concentration (\pm standard deviation) was $3.63 \pm 2.73 \mu\text{g m}^{-3}$, and the eBC ranged from varying from 0.39 to $12.73 \mu\text{g m}^{-3}$ during
341 the study period. The averaged mass concentration was comparable to that in Lanzhou, another river valley city in China, that
342 was sampled in the same season (5.1 ± 2.1 , Zhao et al., 2019). The lowest value is comparable to other river valley regions such
343 as in Retje in India (Glojek et al., 2022) or in Urumqi River Valley in China (Zhang et al., 2020), however even the highest
344 concentration was much lower than that in other urban regions (Table S5).

345 The diel variations of eBC_{fossil} (Figure 2a) showed a bimodal pattern with two peaks at 9 a.m. and 7 p.m. local time. which are
346 typical peak commuting hours, indicating that there were strong influences from traffic emissions. Due to the reduced traffic
347 flow from 1 a.m. to 5 a.m., eBC_{fossil} decreased slowly. After 5 a.m. passenger vehicles were allowed on the highways in and
348 near Baoji, and eBC_{fossil} started to rise, probably in response to the increased traffic emissions. As the morning commuter traffic
349 increased, eBC_{fossil} reached its first peak at 9 a.m. From then until 11 a.m., eBC_{fossil} declined only slightly because the wind
350 speeds decreased (Figure 2c), which offset the effects of the decreases in traffic. From 11 a.m. to 3 p.m., the increases in the
351 height of the planetary boundary layer (PBLH) (Figure 2d) led to a rapid decrease in eBC_{fossil} . Later the PBLH decreased rapidly,
352 resulting in conditions unfavorable for dispersion, and then eBC_{fossil} rose quickly to the second peak at 7 p.m. After passing the
353 evening peak in traffic, the eBC_{fossil} decreased dramatically.

354 In contrast, the diel variation of eBC_{biomass} (Figure 2b) showed greater influences from meteorological conditions during the
355 daytime, and eBC_{biomass} showed lower concentrations during the day compared with the night. After 6 p.m., increased biomass
356 burning from cooking and residential heating led to the emission of more eBC_{biomass} and the stable PBLH hindered the dispersion
357 of eBC_{biomass} ; these two factors caused the eBC_{biomass} to reach its peak at 8 p.m. At night, the downslope winds from the
358 mountains converged in the valley at night time (Oke et al., 2002) and turned easterly, where the land altitude is lower than at
359 Baoji (Zhao et al., 2015). This led to relatively strong winds (Figure 2c) favored dispersion and caused the measured eBC_{biomass}
360 pollutant levels to decrease.

361 **3.2 The influence of regional and local atmospheric motion on eBC_{fossil} and eBC_{biomass}**

362 The K-means results showed that the four-category solution was appropriate for interpretation as explained above (see also
363 Figure S10). Thus a 2×2 map size was used for the self-organizing map (SOM). The four featured atmospheric motion
364 categories given by SOM (Figure S11) were identified as follows (feature values are in Table 1):

- 365 1. Local-scale dominance (LD): This category featured high R_{bj} and R_{std} . As described in section 2.5, high R_{std} indicates
366 greater divergence of R at the 12 stations due to the strong influence of local-scale turbulence and convection. L_{bj} and S_{bj}
367 were shorter than 130 km implying stagnation (Allwine and Whiteman, 1994).

- 368 2. Local-scale strong and regional-scale weak (LSRW): For this group, L_{bj} and S_{bj} were longer than those for LD, and R_{std}
 369 was slightly lower than that in LD.
- 370 3. Local-scale weak and regional-scale strong (LWRS): As the values suggest, both R_{bj} and R_{std} were lower than those in LD
 371 and LSRW, especially R_{bj} . This suggests the winds veered less frequently and the differences of R found in 12 stations
 372 were smaller than in the two situations above. This situation shows that the influence of the regional-scale motion was
 373 greater than that for the previous two categories.
- 374 4. Regional-scale dominance (RD): In this category, wind direction at the study site was nearly uniform (extremely low R_{bj})
 375 suggesting good ventilation (Allwine and Whiteman, 1994). The differences among R found at the 12 stations were even
 376 smaller than for the LWRS group, implying a strong increased influence of regional-scale motions. Indeed, the influence
 377 of regional-scale motions far outweighed the local ones for this category, and therefore, this group was considered to be
 378 dominated by strong regional-scale motions.

379 As shown in Table 1, the SOM classified 40% of cases were classified as LD, 29% were classified into RD, 17% and 14%
 380 were assigned into LSRW and LWRS respectively. These results indicate that most winter days in Baoji were strongly
 381 influenced by local-scale motions. Under LD, the average mass concentration of eBC_{fossil} ($3.08 \pm 2.07 \mu g m^{-3}$) and $eBC_{biomass}$
 382 ($1.52 \pm 1.19 \mu g m^{-3}$) were the highest among all four atmospheric categories noted above and over half (60% for $eBC_{biomass}$ and
 383 55% for eBC_{fossil}) of the high values (75th to 100th percentile) were found in this category (Figure 3). In addition, as shown in
 384 Figure 3, the vast majority of the high values are located in the zone indicating air stagnation ($S_{bj} \leq 130 km$, shaded yellow).
 385 One difference that the 75th to 100th percentile $eBC_{biomass}$ tended to cluster at $R_{bj} \leq 0.2$ indicates that under LD circumstances,
 386 pollutants were likely coming from the same directions as where the main pollution sources were agglomerated, but eBC_{fossil} ,
 387 in contrast, evidently originated from more scattered locations ($R_{bj} \geq 0.4$). Under LSRW, the averaged mass concentrations of
 388 eBC_{fossil} and $eBC_{biomass}$ were $2.79 \pm 1.73 \mu g m^{-3}$ and $1.06 \pm 0.83 \mu g m^{-3}$ respectively (Table 1), which were both lower than those
 389 for the LD situation. When the regional scale of motion became stronger (i.e., LWRS and RD), the average mass concentration
 390 of eBC_{fossil} ($2.15 \pm 1.62 \mu g m^{-3}$ and $1.69 \pm 1.36 \mu g m^{-3}$) and $eBC_{biomass}$ ($0.86 \pm 1.58 \mu g m^{-3}$ and $0.93 \pm 0.72 \mu g m^{-3}$) were lower,
 391 presumably because strong winds cause the pollutants to mix with cleaner air. Interestingly, 19% of the total 75th to 100th
 392 percentile $eBC_{biomass}$ was found under RD, and 55% of that was when ventilation was good ($S_{bj} \geq 250 km$, $R_{bj} \leq 0.2$, Figure 3,
 393 shaded grey). These findings imply that the high mass concentrations of $eBC_{biomass}$ were carried by regional-scale airflow to
 394 the site.

395 Figure 4 portrays the mass concentrations of eBC_{fossil} and $eBC_{biomass}$ during the daytime and night time respectively under the
 396 four atmospheric motion categories specified earlier. As shown in Figure 4 (a) and (c), the mean values of both types of source-
 397 specific eBCs during daytime were the highest ($3.02 \pm 2.12 \mu g m^{-3}$ and $1.15 \pm 0.8 \mu g m^{-3}$) under LD and the lowest ($1.36 \pm$
 398 $1.00 \mu g m^{-3}$ and $0.58 \pm 0.53 \mu g m^{-3}$) under RD. Meanwhile, the average mass concentrations of both types of eBC decreased
 399 when the influences of the regional scale of atmospheric motion getting were stronger. This suggests that eBC pollution was
 400 apt to accumulated under the dominance of local-scale motions and dispersed under the dominance of regional-scale motions
 401 during the daytime. Similar to the variations in the daytime, the mean values of eBC_{fossil} ($3.00 \pm 2.04 \mu g m^{-3}$) and $eBC_{biomass}$
 402 ($1.76 \pm 1.33 \mu g m^{-3}$) under LD were also the highest during the night. However, unlike eBC_{fossil} , the mass concentrations of
 403 $eBC_{biomass}$ did not decrease when the influence of regional-scale atmospheric motions was stronger (Figure S12). The mean

404 value of eBC_{biomass} under RD was the second highest ($1.17 \pm 0.73 \mu\text{g m}^{-3}$). The nocturnal PBHL was higher than 100m (Figure
405 S13) for the RD group, and therefore, the high nocturnal eBC_{biomass} may have been caused by the eBC_{biomass} transported to the
406 site from upwind regions.

407 3.3 Impacts of air mass directions

408 Atmospheric motions can not only cause the dispersal of pollution but also bring polluted air to the site from distant sources.
409 Indeed, air mass movements can mean the difference between no pollution and severe pollution at a receptor site. To examine
410 the impacts caused by air masses from different directions, the hourly 24h-back trajectories were calculated at 100 m above the
411 ground using the Hybrid Single-Particle Lagrangian Integrated Trajectory model (Draxler and Hess, 1998, Text S2). Then the
412 trajectories were clustered by using an angle-based distance statistics method (Text S2) to show the general directional features.
413 This method determines the direction from which the air masses reach the site and has been widely used for air mass trajectory
414 clusters. A detailed method description can be found in Sirois and Bottenheim (1995). Three air-mass trajectory clusters were
415 identified (Figure S14), 45% of total trajectories associated with Cluster No.1, which originated from the north. Cluster No.2
416 accounted for 36% of the trajectories, and those were from the east direction while Cluster No.3 composed 19% of the total
417 trajectories and displayed origins from southwest.

418 Hourly trajectories were assigned into the four featured atmospheric motions. The varying concentrations of the source-specific
419 eBCs associated with different clusters indicate the divergent impacts of air mass direction on the pollution level at the sampling
420 site. As shown in Table 1, LD was mainly connected with the air masses from Cluster No.2 (52%) and Cluster No.1 (45%).
421 The average mass concentrations of eBC_{fossil} and eBC_{biomass} associated with Cluster No.1 were $2.82 \pm 1.59 \mu\text{g m}^{-3}$ and $1.34 \pm$
422 $1.07 \mu\text{g m}^{-3}$. In comparison, Cluster No.2 was associated with a higher mean eBC_{fossil} ($3.2 \pm 1.73 \mu\text{g m}^{-3}$) and the highest mean
423 eBC_{biomass} ($1.72 \pm 1.29 \mu\text{g m}^{-3}$) of the three clusters. This could be attributed to more intensive emissions in the eastern parts of
424 Baoji because 75% of the total population of Baoji is located in this area
425 (http://tjj.baoji.gov.cn/art/2020/10/15/art_9233_1216737.html, accessed on 25 September 2021, in Chinese). Several highways
426 and railways are located in the south and southwest of Baoji, but the population is sparse with only ~4% of the total population
427 residing in those areas. Thus, Cluster No.3 was associated with the highest mean eBC_{fossil} concentration ($3.64 \pm 0.67 \mu\text{g m}^{-3}$)
428 but the lowest mean eBC_{biomass} ($0.67 \pm 0.87 \mu\text{g m}^{-3}$). It is important to point out, however, that only 3% of the total trajectories
429 came from this cluster.

430 Under LSRW, 56% of the trajectories were from Cluster No.1, 33% from Cluster No.2, and 11% from Cluster No.3. Although
431 the total averaged mass concentrations (Table 1) of two types of eBC generally showed that the regional-scale motions favored
432 dissipation of eBC compared with LD, the eBC_{fossil} ($3.43 \pm 1.17 \mu\text{g m}^{-3}$) associated with Cluster No.2 and eBC_{biomass} associated
433 with Cluster No.3. ($1 \pm 0.64 \mu\text{g m}^{-3}$) were higher by $0.23 \mu\text{g m}^{-3}$ and $0.33 \mu\text{g m}^{-3}$ respectively relative to the LD case. The rise
434 of eBC_{fossil} associated with Cluster No.2 was possibly caused by the enhanced regional influence of pollutants brought from
435 adjacent regions. According to previous studies (Wang et al., 2016; Xu et al., 2016), severe BC pollution in winter is caused
436 by fossil fuel combustion in Xi'an which is to the east of Baoji. Studies also have reported that high EC emitted from biomass
437 burning was found to have originated from Sichuan Province (Wu et al., 2020; Cai et al., 2018; Huang et al., 2020) which is to
438 the southwest of Baoji. Combined with the phenomenon that the mass concentration of eBC_{biomass} associated with Cluster No.3

439 rose with regional scales of motion, it is reasonable to conclude that the increase of eBC_{biomass} associated with Cluster No.3 was
440 likely influenced by pollution transport from the southwest.

441 Under LWRS, 42% of the trajectories were from Cluster No.1., 36% from Cluster No.3, and 22% from Cluster No.2. With
442 stronger regional scales of motion, the mean values of eBC_{fossil} and eBC_{biomass} associated with all clusters were lower than those
443 under LD, except for eBC_{biomass} associated with Cluster 3 which increased by $0.52 \mu\text{g m}^{-3}$. As mentioned before, this increase
444 could have been caused by regional transport.

445 In the last category (RD), 41% of the trajectories were from Cluster No.1., 39% from Cluster No.3, and 20% from Cluster No.2.
446 Similar to the results for LWRS, the average mass concentration of eBC_{fossil} and eBC_{biomass} associated with Cluster No.1 were
447 only 35% and 48% of the respective values for LD. The average mass concentrations of eBC_{fossil} and eBC_{biomass} associated with
448 Cluster No.2 were 32% and 51% of the eBC_{fossil} and eBC_{biomass} under LD. As for Cluster No.3, the average mass concentration
449 of eBC_{fossil} associated with this cluster was also the lowest of all clusters. However, interestingly, the mean value of eBC_{biomass}
450 associated with Cluster No.3 was highest compared with other categories of Cluster No.3. Under strong influences of a regional
451 scale of motions, the value of eBC_{biomass} was 1.9 times as high as that under LD.

452 3.4 Radiative effects

453 Figure 5a shows the DREs at top of the atmosphere ($DRE_{\text{eBC, TOA}}$), surface ($DRE_{\text{eBC, SUF}}$), and the whole atmosphere ($DRE_{\text{eBC, ATM}}$)
454 of eBC_{fossil} and eBC_{biomass} . The $DRE_{\text{eBC, TOA}}$ and $DRE_{\text{eBC, SUF}}$ of eBC were 13 W m^{-2} and -22.9 W m^{-2} , which were lower
455 than that reported in Lanzhou (21.8 W m^{-2} and -47.5 W m^{-2} for $DRE_{\text{eBC, TOA}}$ and $DRE_{\text{eBC, SUF}}$) which is another a river valley
456 city in China (Zhao et al., 2019). This could be due to fact that the eBC mass concentration in Baoji was lower than in Lanzhou
457 (Table S5). As for the $DRE_{\text{eBC, TOA}}$ and $DRE_{\text{eBC, SUF}}$ per an unit mass of BC, the results of the two studies were comparable. The
458 $DRE_{\text{eBC, TOA}}$ of eBC_{fossil} ($DRE_{\text{eBCfossil, TOA}}$) and eBC_{biomass} ($DRE_{\text{eBCbiomass, TOA}}$) were $9.4 \pm 7.5 \text{ W m}^{-2}$ and $3.6 \pm 3.4 \text{ W m}^{-2}$ indicating
459 a warming effect at the top of the atmosphere. The $DRE_{\text{eBC, SUF}}$ of eBC_{fossil} ($DRE_{\text{eBCfossil, SUF}}$) and eBC_{biomass} ($DRE_{\text{eBCbiomass, SUF}}$)
460 were $-16.5 \pm 13.5 \text{ W m}^{-2}$ and $-6.4 \pm 6.2 \text{ W m}^{-2}$ showing a cooling effect at the surface. The $DRE_{\text{eBC, ATM}}$ of eBC_{fossil} ($DRE_{\text{eBCfossil, ATM}}$)
461 and eBC_{biomass} ($DRE_{\text{eBCbiomass, ATM}}$) were $25.9 \pm 20.8 \text{ W m}^{-2}$ and $10 \pm 9.5 \text{ W m}^{-2}$ in the atmosphere, indicating a heating
462 effect.

463 Figure 5 also shows the $DRE_{\text{eBC, ATM}}$ of the source-specific eBC for different atmospheric motions. In general, the changes of
464 $DRE_{\text{eBC, ATM}}$ are in accordance with those of the eBC mass concentrations. The $DRE_{\text{eBCfossil, ATM}}$ under LD was the largest with
465 a mean value of $30.4 \pm 23 \text{ W m}^{-2}$, followed by LSRW ($28.7 \pm 20.7 \text{ W m}^{-2}$). As the mass concentration of eBC_{fossil} was low
466 when regional scales of motion were stronger, the $DRE_{\text{eBC, ATM}}$ under LWRS and RD were also lower compared with those
467 under LD or LSRW. By contrast, the $DRE_{\text{eBC, ATM}}$ of eBC_{biomass} under LSRW was the highest ($11.5 \pm 11.8 \text{ W m}^{-2}$), but it is only
468 0.3 W m^{-2} higher than that under LD. When the regional scale of motions became stronger, the $DRE_{\text{eBCbiomass, ATM}}$ declined as
469 expected due to the lower eBC_{biomass} mass concentrations (Figure 4c). The $DRE_{\text{eBC, ATM}}$ of eBC_{biomass} under LWRS and RD were
470 $8.6 \pm 8.5 \text{ W m}^{-2}$ and $7.9 \pm 7.4 \text{ W m}^{-2}$ respectively.

471 Although $DRE_{\text{eBC, ATM}}$ declined with increased influences from the regional scale of motion, the $DRE_{\text{eBC, ATM}}$ efficiency
472 ($DRE_{\text{eBC, ATM}}$ per mass concentration) was found to increase with greater regional-scale motion. Furthermore, the DRE
473 efficiencies of both types of eBC under LD and LSRW were comparable, around 10 W m^{-2} (Table 2). In contrast, the efficiencies

474 varied more when the regional-scale motions were stronger. Under LWRS, the efficiencies of eBC_{fossil} and eBC_{biomass} were 13.5
475 ± 6.7 and 14.7 ± 8.1 ($\text{W m}^{-2}/(\mu\text{g m}^{-3})$) respectively. Under RD, the efficiencies were even higher, 15.6 ± 8.9 ($\text{W m}^{-2}/(\mu\text{g m}^{-3})$)
476 for eBC_{fossil} and 15.5 ± 8.4 ($\text{W m}^{-2}/(\mu\text{g m}^{-3})$) for eBC_{biomass} , which are > 1.5 times those recorded under LD. The higher eBC
477 efficiencies may have been caused by the increases in the BC MAC during the regional transport. Studies have confirmed that
478 the aging processes in the atmosphere can enhance the light-absorbing ability of BC (Chen et al., 2017; Shen et al., 2014), and
479 regional transport can provide sufficient time for BC aging (Shiraiwa, et al. 2007; Cho et al., 2021). Therefore, the nonlinear
480 change between mass concentration and DRE efficiency was very likely caused by the strong regional-scale motions that
481 dispersed fresh BC from local emissions but also brought aged BC to the area from the upwind regions. As a result, under these
482 conditions, the transported BC reached a receptor site with a higher light-absorbing ability which led to a higher DRE efficiency
483 of BC at the sampling site. This strongly implies regionally transported BC can greatly perturb climate, particularly at the river-
484 valley city in our study where dispersion was weak (Zhao et al., 2015; Wang et al., 2013).

485 **4 Conclusions**

486 This study derived site-specific AAEs using a PMF model for which chemical and optical data collected from a river-valley
487 city during winter were used as the inputs. Based on the calculated AAEs, source-specific eBCs (i.e., eBC_{fossil} and eBC_{biomass})
488 were then apportioned using an aethalometer model. Finally, the impacts of different scales of atmospheric motions on the
489 mass concentrations of the source-specific eBCs and the induced DREs were investigated. Four sources of eBC were identified:
490 which are diesel vehicular emissions, biomass burning, coal combustion, and mineral dust. The derived AAEs were 1.07 for
491 diesel vehicular emissions, 2.13 for biomass burning, 1.74 for coal combustion, and 1.78 for mineral dust. The mean values of
492 eBC_{fossil} and eBC_{biomass} were $2.46 \mu\text{g m}^{-3}$ and $1.17 \mu\text{g m}^{-3}$, respectively.

493 The self-organizing map indicated that there were four types of atmospheric motions during the sampling period that affected
494 the mass concentrations of source-specific eBCs. Of these, the local-scale motions were the main influence on most winter
495 days. The eBC_{fossil} and eBC_{biomass} under those identified atmospheric motions showed that over half of the 75th to 100th percentile
496 values for the entire data set were found in LD group (60% for eBC_{biomass} and 55% for eBC_{fossil}). This illustrates that the BC
497 pollution was more severe under the influences of local-scale motion outweighed regional-scale motions. However, even
498 though regional-scale motions were associated with lower eBCs, 19% of the high values of eBC_{biomass} values occurred under
499 RD, especially when there was good ventilation. Furthermore, the air masses from different directions also had impacts on the
500 source-specific eBCs that varied relative to the different atmospheric motions. eBC_{fossil} most likely accumulated under the
501 influence of strong local-scale motions, but eBC_{biomass} also was found to be increased with the enhanced regional scale of
502 motions when the air masses from the southwest; this indicates that there were impacts from regional transport.

503 Similar to the mass concentrations, the DREs of the two types of eBC were both lower when the regional scale of motions were
504 greater than the local ones. However, the changes in mass concentrations and DREs were not proportionate because the
505 regional-scale of motions carried the fresh BC away from the local site but brought the aged BCs to the site from the upwind
506 regions. As a result, the DRE efficiency of eBC was ~ 1.5 times higher when the regional scale of motion was stronger. This
507 study showed that different scales of air motions affected the mass concentrations of source-specific eBCs and their DRE
508 efficiencies. More specifically our study highlights importance of regional transport for the BC radiative forcing and shows

509 how the enhancement of BC radiative effects caused by aging during regional transport could have especially significant
510 implications for sites in river valleys. The relationships between BC and atmospheric scales of motion should be evaluated for
511 other environments besides river valley cities because quantitative information on the relative importance of locally emitted
512 versus regionally transported materials will be useful for developing pollution controls and for predicting future changes in
513 climate.

514 *Data availability.* The data are available from the authors upon request.

515 *Supplement.* The supplement related to this article is available online.

516 *Author contributions.* QW and JC designed the study. BZ and SL conducted the field measurements. YQ and JT conducted
517 data analysis. SL and TZ performed the chemical analysis of filters. HL draft the article and QW revised it. JC and YH
518 commented on the paper.

519 *Competing interests.* The authors declare that they have no conflict of interest.

520 *Acknowledgments.* This research has been supported by the National Natural Science Foundation of China (42192512), the
521 Key Research and Development Program of Shaanxi Province (2018-ZDXM3-01), the Key Project of CAS (ZDRW-ZS-2017-
522 6), and the Youth Innovation Promotion Association of the Chinese Academy of Sciences (2019402).

523 Reference

524 Amato, F., Alastuey, A., Karanasiou, A., Lucarelli, F., Nava, S., Calzolari, G., Severi, M., Becagli, S., Gianelle, V. L., Colombi,
525 C., Alves, C., Custódio, D., Nunes, T., Cerqueira, M., Pio, C., Eleftheriadis, K., Diapouli, E., Reche, C., Minguillón, M.
526 C., Manousakas, M.-I., Maggos, T., Vratolis, S., Harrison, R. M., and Querol, X.: AIRUSE-LIFE+: a harmonized PM
527 speciation and source apportionment in five southern European cities, *Atmos. Chem. Phys.*, 16, 3289–3309,
528 <https://doi.org/10.5194/acp-16-3289-2016>, 2016.

529 Artaxo, P., Fernandes, E. T., Martins, J. V., Yamasoe, M. A., Maenhaut, W., Longo, K. M., Castanho, A., and Hobbs, P. V.:
530 Large-scale aerosol source apportionment in Amazonia, *J. Geophys. Res.-Atmos.*, 103, 31837–31847,
531 <https://doi.org/10.1029/98jd02346>, 1998.

532 Allwine, K. J., and Whiteman, C. D.: Single-station integral measures of atmospheric stagnation, recirculation and ventilation.
533 *Atmos. Environ.*, 28: 713–721, [https://doi.org/10.1016/1352-2310\(94\)90048-5](https://doi.org/10.1016/1352-2310(94)90048-5), 1994.

534 Bei, N., Li, G., Huang, R., Cao, J., Meng, N., Feng, T., Liu, S., Zhang, T., Zhang, Q., and Molina, L.: Typical synoptic situations
535 and their impacts on the wintertime air pollution in the Guanzhong basin, China, *Atmos. Chem. Phys.*, 16, 7373–7387,
536 <http://dx.doi.org/10.5194/acp-16-7373-2016>, 2016.

537 Bond, T. C., Doherty, S. J., Fahey, D. W., Forster, P. M., Berntsen, T., DeAngelo, B. J., Flanner, M. G., Ghan, S., Karcher, B.,
538 Koch, D., Kinne, S., Kondo, Y., Quinn, P. K., Sarofim, M. C., Schultz, M. G., Schulz, M., Venkataraman, C., Zhang, H.,
539 Zhang, S., Bellouin, N., Guttikunda, S. K., Hopke, P. K., Jacobson, M. Z., Kaiser, J. W., Klimont, Z., Lohmann, U.,
540 Schwarz, J. P., Shindell, D., Storelvmo, T., Warren, S. G., and Zender, C. S.: Bounding the role of black carbon in the
541 climate system: A scientific assessment, *J. Geophys. Res.-Atmos.*, 118, 5380–5552, <https://doi.org/10.1002/jgrd.50171>,
542 2013.

543 Brown, S. G., Eberly, S., Paatero, P., and Norris, G. A.: Methods for estimating uncertainty in PMF solutions: Examples with
544 ambient air and water quality data and guidance on reporting PMF results, *Sci. Total Environ.*, 518–519, 626–635,
545 <https://doi.org/10.1016/j.scitotenv.2015.01.022>, 2015.

546 Brulfert, G., Chemel, C., Chaxel, E., Chollet, J., Jouve, B., and Villard, H.: Assessment of 2010 air quality in two Alpine valleys
547 from modelling: weather type and emission scenarios, *Atmos. Environ.*, 40, 7893–7907,
548 <https://doi.org/10.1016/j.atmosenv.2006.07.021>, 2006.

- 549 Cao, J. J., Zhu, C. S., Tie, X. X., Geng, F. H., Xu, H. M., Ho, S. S. H., Wang, G. H., Han, Y. M., and Ho, K. F.: Characteristics
550 and sources of carbonaceous aerosols from Shanghai, China, *Atmos. Chem. Phys.*, 13, 803-817,
551 <https://doi.org/10.5194/acp-13-803-2013>, 2013.
- 552 Cai, S., Ma, Q., Wang, S., Zhao, B., Brauer, M., Cohen, A., Martin, R., Zhang, Q., Li, Q., Wang, Y., Hao, J., Frostad, J.,
553 Forouzanfar, M., and Burnett, R.: Impact of air pollution control policies on future PM_{2.5} concentrations and their source
554 contributions in China, *J. Environ. Manage.*, 227, 124–133, <https://doi.org/10.1016/j.jenvman.2018.08.052>, 2018.
- 555 Cappa, C. D., Onasch, T. B., Massoli, P., Worsnop, D. R., Bates, T. S., Cross, E. S., Davidovits, P., Hakala, J., Hayden, K. L.,
556 Jobson, B. T., Kolesar, K. R., Lack, D. A., Lerner, B. M., Li, S.-M., Mellon, D., Nuaaman, I., Olfert, J. S., Petäjä, T.,
557 Quinn, P. K., Song, C., Subramanian, R., Williams, E. J., and Zaveri, R. A.: Radiative absorption enhancements due to
558 the mixing state of atmospheric black carbon, *Science*, 337, 1078–1081, <https://doi.org/10.1126/science.1223447>, 2012.
- 559 Carvalho, A.C., Carvalho, A., Gelpi, I., Barreiro, M., Borrego, C., Miranda, A., and Perez-Munuzuri, V.: Influence of
560 topography and land use on pollutants dispersion in the Atlantic coast of Iberian Peninsula, *Atmos. Environ.*, 40,3969–
561 3982, <https://doi.org/10.1016/j.atmosenv.2006.02.014>, 2006.
- 562 Cho, C., Schwarz, J., Perriing, A., Lamb, K., Kondo, Y., Park, J., Park, D., Shim, K., Park, J., Park, R., Lee, M., Song, C., Kim,
563 S.: Light-absorption enhancement of black carbon in the Asian outflow inferred from airborne SP2 and in-situ
564 measurements during KORUS- AQ, *Sci. Total Environ.*, 773, 145531, <https://doi.org/10.1016/j.scitotenv.2021.145531>,
565 2021.
- 566 Chang, F., Chang, L., Kang, C., Wang, Y., Huang, A.: Explore spatio-temporal PM_{2.5} features in northern Taiwan using
567 machine learning techniques, *Sci. Total Environ.*, 736, 139656, <https://doi.org/10.1016/j.scitotenv.2020.139656>, 2020.
- 568 Cheng, Y., He, K., Zheng, M., Duan, F., Ma, Y., Tan, J., Yang, F., Liu, J., Zhang, X., Weber, R., Bergin, M. and Russell, A.:
569 Mass absorption efficiency of elemental carbon and water-soluble organic carbon in Beijing, China, *Atmos. Chem. Phys.*,
570 11, 11497–11510, <https://doi.org/10.5194/acp-11-11497-2011>, 2011.
- 571 Chen, X., Wang, Z., Yu, F., Pan, X., Li, J., Ge, B., Wang, Z., Hu, M., Yang, W., Chen, H.: Estimation of atmospheric aging
572 time of black carbon particles in the polluted atmosphere over central-eastern China using microphysical process analysis
573 in regional chemical transport model, *Atmos. Environ.*, 163,44-56, <https://doi.org/10.1016/j.atmosenv.2017.05.016>, 2017
- 574 Drinovec, L., Močnik, G., Zotter, P., Prévôt, A. S. H., Ruckstuhl, C., Coz, E., Rupakheti, M., Sciare, J., Müller, T.,
575 Wiedensohler, A., and Hansen, A. D. A.: The "dual-spot" Aethalometer: an improved measurement of aerosol black
576 carbon with real-time loading compensation, *Atmos. Meas. Tech.*, 8, 1965-1979, <https://doi.org/10.5194/amt-8-1965-2015>,
577 2015.
- 578 Draxler, R., and Hess, G.: An overview of the HYSPLIT_4 modelling system for trajectories, *Aust. Meteorol. Mag.*, 47, 1998.
- 579 Dutton, J., *The ceaseless wind an introduction to the theory of atmospheric motion*, McGraw-Hill, Inc., U.S.A., 1976
- 580 Geivanidis, S., Pistikopoulos, P., and Samaras, Z.: Effect on exhaust emissions by the use of methylcyclopentadienyl
581 manganese tricarbonyl (MMT) fuel additive and other lead replacement gasolines. *Sci. Total Environ.*, 305, 129-141,
582 [https://doi.org/10.1016/S0048-9697\(02\)00476-X](https://doi.org/10.1016/S0048-9697(02)00476-X), 2003.
- 583 Glojek, K., Močnik, G., Alas, H., Cuesta-Mosquera, A., Drinovec, L., Gregorič, A., Ogrin, M., Ježek, I., Müller, T., Rigler,
584 M., Remškar, M., Pinxteren, D., Herrmann, H., Ristorini, M., Merkel, M., Markelj, M., Wiedensohler, A.: The impact of
585 temperature inversions on black carbon and particle mass concentrations in a mountainous area, *Atmos. Chem. Phys.*, 22,
586 5577–5601, <https://doi.org/10.5194/acp-22-5577-2022>, 2022.
- 587 Green, M., Chow, J., and Watson, G.: Effects of snow cover and atmospheric stability on winter PM_{2.5} concentrations in western
588 U.S. valleys, *J. Appl. Meteorol. Clim.*, 54, <https://doi.org/doi:10.1175/JAMC-D-14-0191.1>, 2016.
- 589 Han, H., Liu, J., Shu, L., Wang, T., and Yuan, H.: Local and synoptic meteorological influences on daily variability in
590 summertime surface ozone in eastern China, *Atmos. Chem. Phys.*, 20, 203–222, <https://doi.org/10.5194/acp-20-203-2020>,
591 2020.
- 592 Helin, A., Niemi, J. V., Virkkula, A., Pirjola, L., Teinilä, K., Backman, J., Aurela, M., Saarikoski, S., Rönkkö, T., Asmi, E.,
593 and Timonen, H.: Characteristics and source apportionment of black carbon in the Helsinki metropolitan area, Finland,
594 *Atmos. Environ.*, 190, 87-98, <https://doi.org/10.1016/j.atmosenv.2018.07.022>, 2018.

- 595 He, C., Liou, K.-N., Takano, Y., Zhang, R., Levy Zamora, M., Yang, P., Li, Q., and Leung, L. R.: Variation of the radiative
596 properties during black carbon aging: theoretical and experimental intercomparison, *Atmos. Chem. Phys.*, 15, 11967–
597 11980, <https://doi.org/10.5194/acp-15-11967-2015>, 2015.
- 598 Hewitson, B. C. and Crane, R. G.: Consensus between GCM climate change projections with empirical downscaling:
599 precipitation downscaling over South Africa, *Int. J. Climatol.*, 26, 1315–1337, <https://doi.org/10.1002/joc.1314>, 2006.
- 600 Hsu, C.-Y., Chiang, H.-C., Lin, S.-L., Chen, M.-J., Lin, T.-Y., and Chen, Y.-C.: Elemental characterization and source
601 apportionment of PM₁₀ and PM_{2.5} in the western coastal area of central Taiwan, *Sci. Total Environ.*, 541, 1139–1150,
602 <https://doi.org/10.1016/j.scitotenv.2015.09.122>, 2016.
- 603 Huang, Y., Zhang, L., Li, T., Chen, Y., and Yang, F.: Seasonal variation of carbonaceous species of PM_{2.5} in a small city in
604 Sichuan Basin, China, *Atmosphere.*, 11, 1286, <https://doi.org/10.3390/atmos11121286>, 2020.
- 605 Jacobson, M. Z.: Control of fossil-fuel particulate black carbon and organic matter, possibly the most effective method of
606 slowing global warming, *J. Geophys. Res.*, 107, 4410, <https://doi.org/10.1029/2001JD001376>, 2002.
- 607 Jiang, N. B., Scorgie, Y., Hart, M., Riley, M. L., Crawford, J., Beggs, P. J., Edwards, G. C., Chang, L. S., Salter, D., and
608 Virgilio, G. D.: Visualising the relationships between synoptic circulation type and air quality in Sydney, a subtropical
609 coastal-basin environment, *Int. J. Climatol.*, 37, 1211–1228, <https://doi.org/10.1002/joc.4770>, 2017.
- 610 Kant, Y., Shaik, D., S., Mitra, D., Chandola, H., Babu, S. S., and Chauhan, P., Black carbon aerosol quantification over north-
611 west himalayas: seasonal heterogeneity, source apportionment and radiative forcing, *Environ. Pollut.*,
612 10.1016/j.envpol.2019.113446, 2019.
- 613 Kangas, J., and Kohonen, T.: Developments and applications of the self-organizing map and related algorithms, *Math. Comput.*
614 *Simulat.*, 41, 3-12, [https://doi.org/10.1016/0378-4754\(96\)88223-1](https://doi.org/10.1016/0378-4754(96)88223-1), 1996.
- 615 Kahnert, M., and Kanngiesser, F.: Review: modelling optical properties of atmospheric black carbon aerosols. *J. Quant.*
616 *Spectrosc., RA*, 244, 106849, <https://doi.org/10.1016/j.jqsrt.2020.106849>, 2020.
- 617 Kalthoff, N., Horlacher, V., Corsmeier, U., Volz-Thomas, A., Kolahgar, B., Geiß, H., Möllmann-Coers, M., and Knaps, A.:
618 Influence of valley winds on transport and dispersion of airborne pollutants in the Freiburg-Schauinsland area, *J. Geophys.*
619 *Res.-Atmos.*, 105, 1585–1597, <https://doi.org/10.1029/1999jd900999>, 2000.
- 620 Kirchstetter, T. W., Novakov, T., and Hobbs, P. V.: Evidence that the spectral dependence of light absorption by aerosols is
621 affected by organic carbon, *J. Geophys. Res.-Atmos.*, 109, D21208, <https://doi.org/10.1029/2004jd004999>, 2004.
- 622 Kohonen, T.: The self-organizing map, *Proc. IEEE*, 78, 1464–1480, <https://doi.org/10.1109/5.58325>, 1990.
- 623 Kohonen, T., and Simula, O., Visa, A., Kangas, J.: Engineering applications of the self-organizing map, *P. IEEE*, 84(10), 1358-
624 1384, <https://doi.org/10.1109/5.537105>, 1996.
- 625 Liao, Z., Xie, J., Fang, X., Wang, Y., Zhang, Y., Xu, X., and Fan, S.: Modulation of synoptic circulation to dry season PM_{2.5}
626 pollution over the Pearl River Delta region: An investigation based on self-organizing maps. *Atmos. Environ.*, 230, 117482,
627 <https://doi.org/10.1016/j.atmosenv.2020.117482>, 2020.
- 628 Liu, S., Gautam, A., Yang, X., Tao, J., Wang, X., Zhao, W: Analysis of improvement effect of PM_{2.5} and gaseous pollutants in
629 Beijing based on self-organizing map network, *Sustain. Cities Soc.*, 70, 102827, <https://doi.org/10.1016/j.scs.2021.102827>,
630 2021.
- 631 Lewis, C. W., Norris, G. A., Conner, T. L., and Henry, R. C.: Source apportionment of Phoenix PM_{2.5} aerosol with the unmix
632 receptor model, *J. Air Waste Manage.*, 53, 325–338, <https://doi.org/10.1080/10473289.2003.10466155>, 2003.
- 633 Levy, I., Dayan, U., and Mahrer, Y.: Differing atmospheric scales of motion and their impact on air pollutants, *Int. J. Climatol.*,
634 30, 612–619, <https://doi.org/10.1002/joc.1905>, 2010.
- 635 Lin, Y., Tsai, C., Wu, T., Zhang, R., Chi, K., Huang, Y., Lin, S., and Hsu, S.: Characteristics of trace metals in traffic-derived
636 particles in Hsuehshan Tunnel, Taiwan: size distribution, potential source, and fingerprinting metal ratio, *Atmos. Chem.*
637 *Phys.*, 15, 4117–4130, <https://doi.org/10.5194/acp-15-4117-2015>, 2015.
- 638 IPCC: Climate Change 2021: The physical science basis. contribution of working group I to the sixth assessment report of the
639 intergovernmental panel on climate change [Masson-Delmotte, V., P. Zhai, A. Pirani, S.L. Connors, C. Péan, S. Berger,

- 640 N. Caud, Y. Chen, L. Goldfarb, M.I. Gomis, M. (eds)], [https://reliefweb.int/report/world/climate-change-2021-physical-](https://reliefweb.int/report/world/climate-change-2021-physical-science-basis)
641 [science-basis](https://reliefweb.int/report/world/climate-change-2021-physical-science-basis), 2021
- 642 Manousakas, M., Papaefthymiou, H., Diapouli E., Migliori, A., Karydas, A.G., Bogdanovic-Radovic, I., Eleftheriadis, K.:
643 Assessment of PM_{2.5} sources and their corresponding level of uncertainty in a coastal urban area using EPA PMF 5.0
644 enhanced diagnostics, *Sci. Total Environ.*, 574, 155–164, <https://doi.org/10.1016/j.scitotenv.2016.09.047>, 2017.
- 645 Manö, S., and Andreae, M.O.: Emission of methyl bromide from biomass burning. *Science.*, 263, 1255–1257,
646 <https://doi.org/10.1126/science.263.5151.1255>, 1994.
- 647 Norris, G., Duvall, R., Brown, S. and Bai, S.: EPA Positive Matrix Factorization (PMF) 5.0 fundamentals and user guide
648 prepared for the US Environmental Protection Agency Office of 30 research and development, Washington, DC, by the
649 National Exposure Research Laboratory, Research Triangle Park; Sonoma Technology, Inc., Petaluma.,
650 <https://www.epa.gov/air-research/epa-positive-matrix-factorization-50-fundamentals-and-user-guide>, 2014.
- 651 Ochoa-Hueso, R., Munzi, S., Alonso, R., Arróniz-Crespo, M., Avila, A., Bermejo, V., Bobbink, R., Branquinho, C.,
652 Concostrina-Zubiri, L., Cruz, C., Cruz de Carvalho, R., De Marco, A., Dias, T., Elustondo, D., Elvira, S., Estébanez, B.,
653 Fusaro, L., Gerosa, G., Izquieta-Rojano, S., Lo Cascio, M., Marzuoli, R., Matos, P., Mereu, S., Merino, J., Morillas, L.,
654 Nunes, A., Paoletti, E., Paoli, L., Pinho, P., Rogers, I.B., Santos, A., Sicard, P., Stevens, C. J., and Theobald, M. R.:
655 Ecological impacts of atmospheric pollution and interactions with climate change in terrestrial ecosystems of the
656 Mediterranean Basin: current research and future directions, *Environ. Pollut.*, 227, 194–206, 2017.
- 657 Oke, T., *Boundary layer climates*, 2nd edition, Taylor & Francis e-Library, 2002.
- 658 Panicker, A. S., Pandithurai, G., Safai, P. D., Dipu, S., and Lee, D.-I.: On the contribution of black carbon to the composite
659 aerosol radiative forcing over an urban environment, *Atmos. Environ.*, 44, 3066-3070, [10.1016/j.atmosenv.2010.04.047](https://doi.org/10.1016/j.atmosenv.2010.04.047),
660 2010.
- 661 Pathak, B., Kalita, G., Bhuyan, K., Bhuyan, P. and Moorthy, K.: Aerosol temporal characteristics and its impact on shortwave
662 radiative forcing at a location in the northeast of India, *J. Geophys. Res.-Atmos.*, 115, D19204,
663 <https://doi.org/10.1029/2009JD013462>, 2010.
- 664 Peng, J., Hu, M., Guo, S., Du, Z., Zheng, J., Shang, D., Levy, M., and Zeng, L.: Markedly enhanced absorption and direct
665 radiative forcing of black carbon under polluted urban environments, *P. Natl. Acad. Sci. USA*, 113, 4266–4271,
666 <https://doi.org/10.1073/pnas.1602310113>, 2016.
- 667 Pearce, J. L., Waller, L. A., Chang, H. H., Klein, M., Mulholland, J. A., Sarnat, J. A., Sarnat, S. E., Strickland, M. J., and
668 Tolbert, P. E.: Using self-organizing maps to develop ambient air quality classifications: a time series example, *Environ.*
669 *Health-Glob.*, 13, <https://doi.org/10.1186/1476-069X-13-56>, 2014.
- 670 Ramachandran A., Rustum, R., and Adeloje, A.: Anaerobic digestion process modeling using Kohonen self-organising maps,
671 *Heliyon*, 5,e01511, <https://doi.org/10.1016/j.heliyon.2019.e01511>, 2019.
- 672 Rajesh, T. A., and Ramachandran, S.: Black carbon aerosols over urban and high altitude remote regions: characteristics and
673 radiative implications, *Atmos. Environ.*, 194, 110-122, <https://doi.org/10.1016/j.atmosenv.2018.09.023>, 2018.
- 674 Reusch, D.B., Alley, R.B., and Hewitson, B.C.: Relative performance of self-organizing maps and principal component analysis
675 in pattern extraction from synthetic climatological data. *Polar Geogr.*, 29(3): 188–212.
676 <http://dx.doi.org/10.1080/789610199>, 2005.
- 677 Ricchiazzi, P., Yang, S., Gautier, C., and Sowle, D.: SBDART: A research and teaching software tool for plane-parallel
678 radiative transfer in the Earth's atmosphere, *B. Am. Meteorol. Soc.*, 79, 2101–2114, [https://doi.org/10.1175/1520-](https://doi.org/10.1175/1520-0477(1998)0792.0.CO;2)
679 [0477\(1998\)0792.0.CO;2](https://doi.org/10.1175/1520-0477(1998)0792.0.CO;2), 1998.
- 680 Sandradewi, J., Prévôt, A. S. H., Weingartner, E., Schmidhauser, R., Gysel, M., and Baltensperger, U.: A study of wood burning
681 and traffic aerosols in an Alpine valley using a multi-wavelength Aethalometer, *Atmos. Environ.*, 42, 101-112,
682 <https://doi.org/10.1016/j.atmosenv.2007.09.034>, 2008.
- 683 Seinfeld, J., and Pandis, S., 2006. *Atmospheric chemistry and physics: from air pollution to climate change*, 2nd ed., Published
684 by John Wiley & Sons, Inc., Hoboken, New Jersey, United States of America,

685 Schroter, D., Cramer, W., Leemans, R., Prentice, C., Araujo, M., Arnell, N., Bondeau, A., Bugmann, H., Carter, T., Gracia, C.,
686 de la Vega-Leinert, A., Erhard, M., Ewert, F., Glendining, M., House, J., Kankaanpaa, S., Klein, R., Lavorel, S., Lindner,
687 M., Metzger, M., Meyer, J., Mitchell, T., Reginster, I., Rounsevell, M., Sabate, S., Sitch, S., Smith, B., Smith, J., Smith,
688 P., Sykes, M., Thonicke, K., Thuiller, W., Tuck, G., Zaehle, S., and Zierl, B.: Ecosystem service supply and vulnerability
689 to global change in Europe, *Science*, 310, 1333–1337, <https://doi.org/10.1126/science.1115233>, 2005.

690 Shen, Z., Liu, J., Horowitz, W., Henze, D., Levy, H., Mauzerall, D., Lin, J., and Tao, S.: Analysis of transpacific transport of
691 black carbon during HIPPO-3: implications for black carbon aging, *Atmos. Chem. Phys.*, 14, 6315–6327,
692 <https://doi.org/10.5194/acp-14-6315-2014>, 2014.

693 Shiraiwa, M., Kondo, Y., Moteki, N., Takegawa, N., Miyazaki, Y., and Blake, D. R.: Evolution of mixing state of black carbon
694 in polluted air from Tokyo, *Geophys. Res. Letters*, 34, L16803, <https://doi.org/10.1029/2007GL029819>, 2007.

695 Shindell, D., Kuylentstierna, J. C. I., Vignati, E., van Dingenen, R., Amann, M., Klimont, Z., Anenberg, S. C., Muller, N.,
696 JanssensMaenhout, G., Raes, F., Schwartz, J., Faluvegi, G., Pozzoli, L., Kupiainen, K., Hoglund-Isaksson, L., Emberson,
697 L., Streets, D., Ramanathan, V., Hicks, K., Oanh, N. T. K., Milly, G., Williams, M., Demkine, V., and Fowler, D.:
698 Simultaneously mitigating near-term climate change and improving human health and food security, *Science*, 335, 183–
699 189, <https://doi.org/10.1126/science.1210026>, 2012.

700 Sirois, A. and Bottenheim, J. W.: Use of backward trajectories to interpret the 5-year record of PAN and O₃ ambient air
701 concentrations at Kejimikujik National Park, Nova Scotia, *J. Geophys. Res.*, 100, 2867–2881,
702 <https://doi.org/10.1029/94JD02951>, 1995.

703 Song, Y., Zhang, Y., Xie, S., Zeng, L., Zheng, M., Salmon, L. G., Shao, M., and Slanina, S.: Source apportionment of PM_{2.5} in
704 Beijing by positive matrix factorization, *Atmos. Environ.*, 40, 1526–1537, <https://doi.org/10.1016/j.atmosenv.2005.10.039>,
705 2006.

706 Sun, J., Zhi, G., Hitzenberger, R., Chen, Y., Tian, C., Zhang, Y., Feng, Y., Cheng, M., Zhang, Y., Cai, J., Chen, F., Qiu, Y.,
707 Jiang, Z., Li, J., Zhang, G., and Mo, Y.: Emission factors and light absorption properties of brown carbon from household
708 coal combustion in China, *Atmos. Chem. Phys.*, 17, 4769–4780, <https://doi.org/10.5194/acp-17-4769-2017>, 2017.

709 Stauffer, R. M., Thompson, A. M., and Young, G. S.: Tropospheric ozonesonde profiles at long-term US monitoring sites: 1.
710 A climatology based on self-organizing maps, *J. Geophys. Res.-Atmos*, 121, 1320–1339,
711 <https://doi.org/10.1002/2015JD023641>, 2016.

712 Tan, J., Zhang, L. Zhou, X., Duan, J. Li, Y., Hu, J., and He, K.: Chemical characteristics and source apportionment of PM_{2.5} in
713 Lanzhou, China, *Sci. Total Environ.*, 601, 1743–1752, <https://doi.org/10.1016/j.scitotenv.2017.06.050>, 2017.

714 Tao, J., Zhang L., Zhang, R., Wu, Y., Zhang, Z., Zhang, X., Tang, Y., Cao, J., and Zhang, Y.: Uncertainty assessment of source
715 attribution of PM_{2.5} and its water-soluble organic carbon content using different biomass burning tracers in positive
716 matrix factorization analysis — a case study in Beijing, China, *Sci. Total Environ.*, 543, 326–335,
717 <https://doi.org/10.1016/j.scitotenv.2015.11.057>, 2016.

718 Tao, J., Zhang, L. M., Cao, J. J., Zhong, L. J., Chen, D. S., Yang, Y. H., Chen, D. H., Chen, L. G., Zhang, Z. S., Wu, Y. F.,
719 Xia, Y. J., Ye, S. Q., and Zhang, R. J.: Source apportionment of PM_{2.5} at urban and suburban areas of the Pearl River Delta
720 region, south China – with emphasis on ship emissions, *Sci. Total Environ.*, 574, 1559–1570,
721 <https://doi.org/10.1016/j.scitotenv.2016.08.175>, 2017.

722 Thorpe, A., and Harrison, R. M.: Sources and properties of non-exhaust particulate matter from road traffic: a review, *Sci.*
723 *Total Environ.*, 400, 270–282, <https://doi.org/10.1016/j.scitotenv.2008.06.007>, 2008.

724 Urban, R. C., Lima-Souza, M., Caetano-Silva, L., Queiroz, M. E. C., Nogueira, R. F. P., Allen, A. G., Cardoso, A. A., Held,
725 G., and Campos, M. L. A. M.: Use of levoglucosan, potassium, and water-soluble organic carbon to characterize the
726 origins of biomass-burning aerosols, *Atmos. Environ.*, 61, 562–569, <https://doi.org/10.1016/j.atmosenv.2012.07.082>, 2012.

727 Washenfelder, R., Attwood, A., Brock, C., Guo, H., Xu, L., Weber, R., Ng, N., Allen, H., Ayres, B., Baumann, K., Cohen, R.,
728 Draper, D., Duffey, K., Edgerton, E., Fry, J., Hu, W., Jimenez, J., Palm, B., Romer, P., Stone, E., Wooldridge, P., and
729 Brown, S.: Biomass burning dominates brown carbon absorption in the rural southeastern United States, *Geophys. Res.*
730 *Let.*, 42, 653–664, <https://doi.org/10.1002/2014GL062444>, 2015

- 731 Wang, Q., Huang, R., Zhao, Z., Cao, J., Ni, H., Tie, X., Zhao, S., Su, X., Han, Y., Shen, Z., Wang, Y., Zhang, N., Zhou, Y.,
732 and Corbin, J.: Physicochemical characteristics of black carbon aerosol and its radiative impact in a polluted urban area
733 of China, *J. Geophys. Res. Atmos.*, 121, <https://doi.org/doi:10.1002/2016JD024748>, 2016.
- 734 Wang, Q., Han, Y., Ye, J., Liu, S., Pongpiachan, S., Zhang, N., Han, Y., Tian, J., Wu, C., Long, X., Zhang, Q., Zhang, W.,
735 Zhao, Z., and Cao, J.: High contribution of secondary brown carbon to aerosol light absorption in the southeastern margin
736 of Tibetan Plateau, *Geophys. Res. Lett.*, 46, 4962–4970, <https://doi.org/10.1029/2019GL082731>, 2019.
- 737 Wang, Q., Liu, H., Wang, P., Dai, W., Zhang T., Zhao, Y., Tian, J., Zhang, W., Han, Y., and Cao, J.: Optical source
738 apportionment and radiative effect of light-absorbing carbonaceous aerosols in a tropical marine monsoon climate zone:
739 the importance of ship emissions, *Atmos. Chem. Phys.*, 20, 15537–15549, <https://doi.org/10.5194/acp-20-15537-2020>,
740 2020.
- 741 Wang, W., Chen, N., and Ma, X., Characteristic analysis on mountain-valley wind in deep valley, *Adv. Mater.*, Vols 610-613,
742 pp 817-824, <https://doi:10.4028/www.scientific.net/AMR.610-613.817>, 2013.
- 743 Wei, N., Wang, N., Huang, X., Liu, P., and Chen, L.: The effects of terrain and atmospheric dynamics on cold season heavy
744 haze in the Guanzhong Basin of China, *Atmos. Pollut. Res.*, 11, 1805-1819, <https://doi.org/10.1016/j.apr.2020.07.007>,
745 2020.
- 746 Wehrens, R., and Kruisselbrink, J.: Supervised and unsupervised self-organising maps, Package ‘kohonen’, 2019,
747 <https://cran.r-project.org/>.
- 748 Wu, J., Kong, S., Wu, F., Cheng, Y., Zheng, S., Qin, S., Liu, X., Yan, Q., Zheng, H., Zheng, M., Yan, Y., Liu, D., Ding, S.,
749 Zhao, D., Shen, G., Zhao, T., and Qi, S.: The moving of high emission for biomass burning in China: view from multiyear
750 emission estimation and human-driven forces, *Environ. Int.*, 142, 105812, <https://doi.org/10.1016/j.envint.2020.105812>,
751 2020.
- 752 Wu, C. and Yu, J. Z.: Determination of primary combustion source organic carbon-to-elemental carbon (OC / EC) ratio using
753 ambient OC and EC measurements: secondary OC-EC correlation minimization method, *Atmos. Chem. Phys.*, 16, 5453–
754 5465, <https://doi.org/10.5194/acp-16-5453-2016>, 2016.
- 755 Xiao, S., Wang, Q., Cao, J., Huang, R., Chen, W., Han, Y., Xu, H., Xu, H., Liu, S., Zhou, Y., Wang, P., Zhang, J., Zhan, C.:
756 Long-term trends in visibility and impacts of aerosol composition on visibility impairment in Baoji, China, *Atmos. Res.*,
757 149, 88–95, <http://dx.doi.org/10.1016/j.atmosres.2014.06.006>, 2014.
- 758 Xu, H. M., Cao, J. J., Ho, K. F., Ding, H., Han, Y. M., Wang, G. H., Chow, J. C., Watson, J. G., Khol, S. D., Qiang, J., and Li,
759 W. T.: Lead concentrations in fine particulate matter after the phasing out of leaded gasoline in Xi’an, China, *Atmos.*
760 *Environ.*, 46, 217– 224, <https://doi.org/10.1016/j.atmosenv.2011.09.078>, 2012.
- 761 Xu, H., Ren, Y., Zhang, W., Meng, W., Yun, X., Yu, X., Li, J., Zhang, Y., Shen, G., Ma, J., Li, B., Cheng, H., Wang, X., Wan,
762 Y., and Tao, S.: Updated global black carbon emissions from 1960 to 2017: improvements, trends, and drivers, *Environ.*
763 *Sci. Technol.*, 55, 7869-7879, <https://doi.org/10.1021/acs.est.1c03117>, 2021.
- 764 Xu, H., Cao, J., Chow, J., Huang, R., Shen, Z., Chen, L.W., Ho, K., Watson, J.: Inter-annual variability of wintertime PM_{2.5}
765 chemical composition in Xi’an, China: evidences of changing source emissions, *Sci. Total Environ.*, 545, 546–555,
766 <http://dx.doi.org/10.1016/j.scitotenv.2015.12.070>, 2016.
- 767 Yan, C., Zheng, M., Sullivan, A., Bosch, C., Desyaterik., Andersson, A., Li, X., Guo, X., Zhou, T., Gustafsson, O., Collett Jr.,
768 J.: Chemical characteristics and light-absorbing property of water soluble organic carbon in Beijing: biomass burning
769 contributions, *Atmos. Environ.*, 121, 4-12, <http://dx.doi.org/10.1016/j.atmosenv.2015.05.005>, 2015.
- 770 Yang, M., Howell, S. G., Zhuang, J., and Huebert, B. J.: Attribution of aerosol light absorption to black carbon, brown carbon,
771 and dust in China – interpretations of atmospheric measurements during EAST-AIRE, *Atmos. Chem. Phys.*, 9, 2035–2050,
772 <https://doi.org/10.5194/acp-9-2035-2009>, 2009.
- 773 Yao, X., Chan, C. K., Fang, M., Cadle, S., Chan, T., Mulawa, P., He, K., and Ye, B.: The water-soluble ionic composition of
774 PM_{2.5} in Shanghai and Beijing, China, *Atmos. Environ.*, 36, 4223–4234, [https://doi.org/10.1016/S1352-2310\(02\)00342-](https://doi.org/10.1016/S1352-2310(02)00342-4)
775 4, 2002.
- 776 Zhao, S., Tian, H., Luo, L., Liu, H., Wu, B., Liu, S., Bai, X., Liu, W., Liu, X., Wu, Y., Lin, S., Guo, Z., Lv, Y., and Xue, Y.:
777 Temporal variation characteristics and source apportionment of metal elements in PM_{2.5} in urban Beijing during 2018–
778 2019, *Environ. Pollut.*, 268, 115856, <https://doi.org/10.1016/j.envpol.2020.115856>, 2021.

779 Zhao, S., Tie, X., Cao, J., and Zhang, Q.: Impacts of mountains on black carbon aerosol under different synoptic meteorology
780 conditions in the Guanzhong region, China, *Atmos. Res.*, 164–165, 286–296,
781 <https://doi.org/10.1016/j.atmosres.2015.05.016>, 2015

782 Zhao, S. P., Yu, Y., Yin, D., Yu, Z., Dong, L. X., Mao, Z., He, J. J., Yang, J., Li, P., and Qin, D. H.: Concentrations, optical
783 and radiative properties of carbonaceous aerosols over urban Lanzhou, a typical valley city: results from in-situ
784 observations and numerical model, *Atmos. Environ.*, 213, 470–484, <https://doi.org/10.1016/j.atmosenv.2019.06.046>, 2019.

785 Zhang, Z., Gao, J., Engling, G., Tao, J., Chai, F., Zhang, L., Zhang, R., Sang, X., Chan, C., Lin, Z., and Cao, J.: Characteristics
786 and applications of size-segregated biomass burning tracers in China's Pearl River Delta region, *Atmos. Environ.*, 102,
787 290–301. <https://doi.org/10.1016/j.atmosenv.2014.12.009>, 2015.

788 Zhang, J. P., Zhu, T., Zhang, Q. H., Li, C. C., Shu, H. L., Ying, Y., Dai, Z. P., Wang, X., Liu, X. Y., Liang, A. M., Shen, H.
789 X., and Yi, B. Q.: The impact of circulation patterns on regional transport pathways and air quality over Beijing and its
790 surroundings, *Atmos. Chem. Phys.*, 12, 5031–5053, <https://doi.org/10.5194/acp-12-5031-2012>, 2012.

791 Zhang, Y., Li, M., Cheng, Y., Geng, G., Hong, C., Li, H., Li, X., Tong, D., Wu, N., Zhang, X., Zheng, B., Zheng, Y., Bo, Y.,
792 Su, H., and Zhang, Q.: Modeling the aging process of black carbon during atmospheric transport using a new approach: a
793 case study in Beijing, *Atmos. Chem. Phys.*, 19, 9663–9680, <https://doi.org/10.5194/acp-19-9663-2019>, 2019.

794 Zhou, B., Wang, Q., Zhou, Q., Zhang, Z., Wang, G., Fang, N., Li, M., Cao, J.: Seasonal characteristics of black carbon aerosol
795 and its potential source regions in Baoji, China, *Aerosol Air. Qual. Res.*, 18, 397–406, <https://doi.org/10.4209/aaqr.2017.02.0070>, 2018.

797 Zotter, P., Herich, H., Gysel, M., El-Haddad, I., Zhang, Y., Močnik, G., Hüglin, C., Baltensperger, U., Szidat, S., and Prévôt,
798 A. S. H.: Evaluation of the absorption Ångström exponents for traffic and wood burning in the Aethalometer-based source
799 apportionment using radiocarbon measurements of ambient aerosol, *Atmos. Chem. Phys.*, 17, 4229–4249,
800 <https://doi.org/10.5194/acp-17-4229-2017>, 2017

801

802
803

Table 1. The mass concentration of eBC from fossil fuel combustion (eBC_{fossil}) and eBC from biomass burning (eBC_{biomass}) associated with different clusters under four featured atmospheric motions

Motion category	Local scale dominance (LD) (40%)				Local scale strong and regional scale weak (LSRW) (17%)			
	L _{bj} = 70.9 km, S _{bj} = 107.8 km, R _{bj} = 0.35, R _{std} = 0.25				L _{bj} = 106.9 km, S _{bj} = 164.8 km, R _{bj} = 0.33, R _{std} = 0.23			
	Cluster 1	Cluster 2	Cluster 3	Total average	Cluster 1	Cluster 2	Cluster 3	Total average
Trajectory percentage (%)	45	52	3	100	56	33	11	100
eBC _{fossil} (µg m ⁻³)	2.82 ^a ± 1.59 ^b	3.2 ± 1.73	3.64 ± 0.67	3.08 ± 2.07	2.42 ± 1.00	3.43 ± 1.17	2.89 ± 1.00	2.79 ± 1.73
eBC _{biomass} (µg m ⁻³)	1.34 ± 1.07	1.72 ± 1.29	0.67 ± 0.87	1.52 ± 1.19	1.0 ± 0.85	1.17 ± 0.84	1.00 ± 0.64	1.06 ± 0.83

804 L_{bj}—resultant transport distance, S_{bj}—actual wind run distance at 100 m, R_{bj}—recirculation factor at 100 m, R_{std}—standard deviation for
805 recirculation factor. a and b: Mean ± Standard deviation.
806

807

Table 1 (continued)

Motion category	Local scale weak and regional scale strong (LWRS) (14%)				Regional scale dominance (RD) (29%)			
	L _{bj} = 159 km, S _{bj} = 183.4 km, R _{bj} = 0.13, R _{std} = 0.20				L _{bj} = 235.6 km, S _{bj} = 246.4 km, R _{bj} = 0.05, R _{std} = 0.18			
	Cluster 1	Cluster 2	Cluster 3	Total average	Cluster 1	Cluster 2	Cluster 3	Total average
Trajectory percentage (%)	42	22	36	100	41	20	39	100
eBC _{fossil} (µg m ⁻³)	1.32 ^a ± 0.67 ^b	2.02 ± 0.73	3.16 ± 1.19	2.15 ± 1.62	1.00 ± 0.64	1.02 ± 0.88	2.75 ± 1.26	1.69 ± 1.36
eBC _{biomass} (µg m ⁻³)	0.67 ± 0.49	0.73 ± 0.47	1.19 ± 0.60	0.86 ± 0.58	0.64 ± 0.63	0.87 ± 0.69	1.26 ± 0.68	0.93 ± 0.72

808 L_{bj}—resultant transport distance, S_{bj}—actual wind run distance at 100 m, R_{bj}—recirculation factor at 100 m, R_{std}—standard
809 deviation for recirculation factor. a and b: Mean ± Standard deviation.

810 **Table 2.** Direct radiative forcing efficiencies for equivalent black carbon (eBC) from fossil fuel combustion (eBC_{fossil}) and the eBC from biomass burning
 811 (eBC_{biomass}) under four atmospheric motion categories

Atmospheric motion category	DRE _{eBCfossil, ATM} efficiency ((W m ⁻²)/(μg m ⁻³))	DRE _{eBCbiomass, ATM} efficiency ((W m ⁻²)/(μg m ⁻³))
Local scale dominance (LD)	10.2 ^a ± 4.2 ^b	10.3 ± 4.4
Local scale strong and regional scale weak (LSRW)	10.6 ± 5.7	10.2 ± 5.8
Local scale weak and regional scale strong (LWRS)	13.5 ± 6.7	14.7 ± 8.1
Regional scale dominance (RD)	15.6 ± 8.9	15.5 ± 8.4

812 a and b: Mean ± Standard deviation

813

814 **Figure captions:**

815 **Figure 1.** Four factors identified by source apportionment. Concentration ($\mu\text{g m}^{-3}$) of the chemical species and primary
816 absorption coefficients (p_{abs}) (λ) at six wavelengths ($\lambda = 370, 470, 520, 590, 660, \text{ or } 880\text{nm}$) (M m^{-1}) for each source are shown
817 in grey. The blue square represents the contribution of each chemical species to the four different factors.

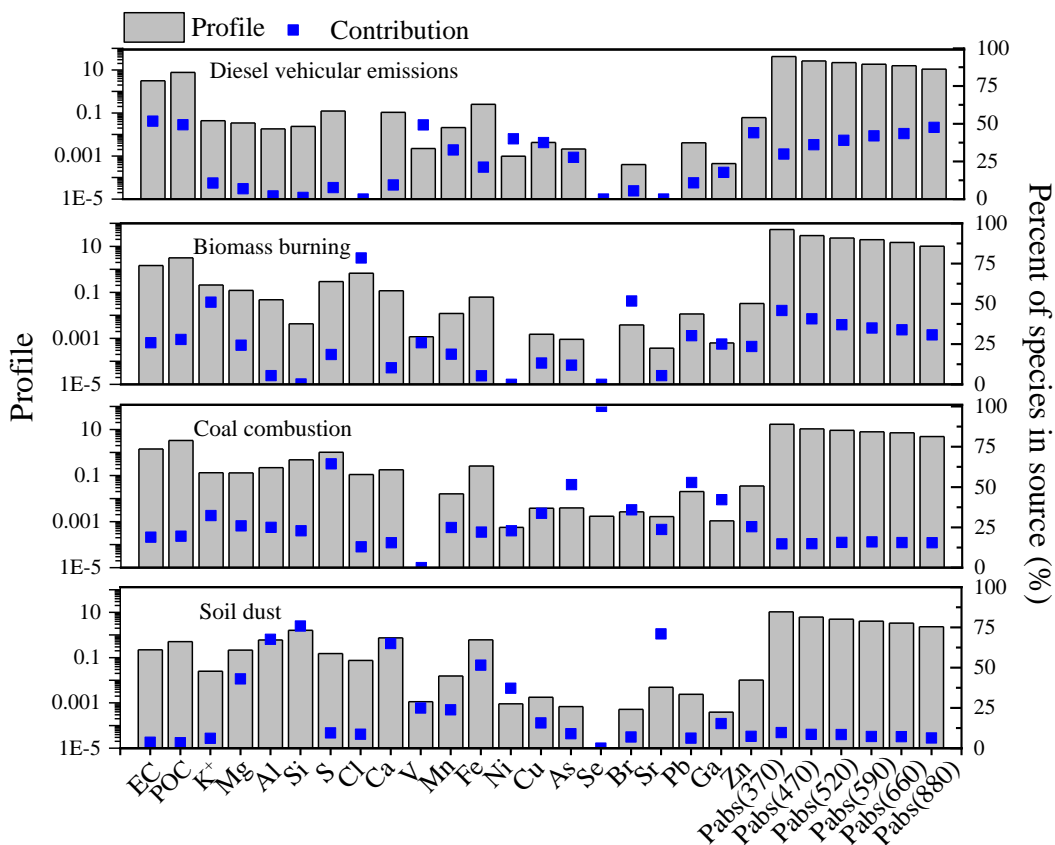
818 **Figure 2.** (a) Diel variations of the eBC from fossil fuel combustion ($\text{eBC}_{\text{fossil}}$) and (b) the eBC from biomass burning
819 ($\text{eBC}_{\text{biomass}}$), (c) wind speed (m s^{-1}) and (d) planetary boundary layer height (m). The black bars of each hourly-averaged point
820 show the standard deviation.

821 **Figure 3.** (a) The 75th – 100th percentile mass concentrations of the eBC from fossil fuel combustion ($\text{eBC}_{\text{fossil}}$) and (b) the eBC
822 from biomass burning ($\text{eBC}_{\text{biomass}}$) under local scale dominance (LD, red circle), local scale strong and regional scale weak
823 (LSRW, green circle), local scale weak regional scale strong (LWRS, purple circle) and regional scale dominance (RD, blue
824 circle). S_{bj} is actual wind run distance at 100m height, R_{bj} is the recirculation factor, the grey area indicates good ventilation
825 ($S_{\text{bj}} \geq 250\text{km}$, $R_{\text{bj}} \leq 0.2$), the yellow area indicates air stagnation ($S_{\text{bj}} \leq 130\text{km}$).

826 **Figure 4.** Mass concentrations of the eBC from fossil fuel combustion ($\text{eBC}_{\text{fossil}}$) and the eBC from biomass burning ($\text{eBC}_{\text{biomass}}$)
827 during daytime (a, c) and nighttime (b, d) under local scale dominance (LD); local scale strong and regional scale weak
828 (LSRW); local scale weak regional strong (LWRS); and regional scale dominance (RD).

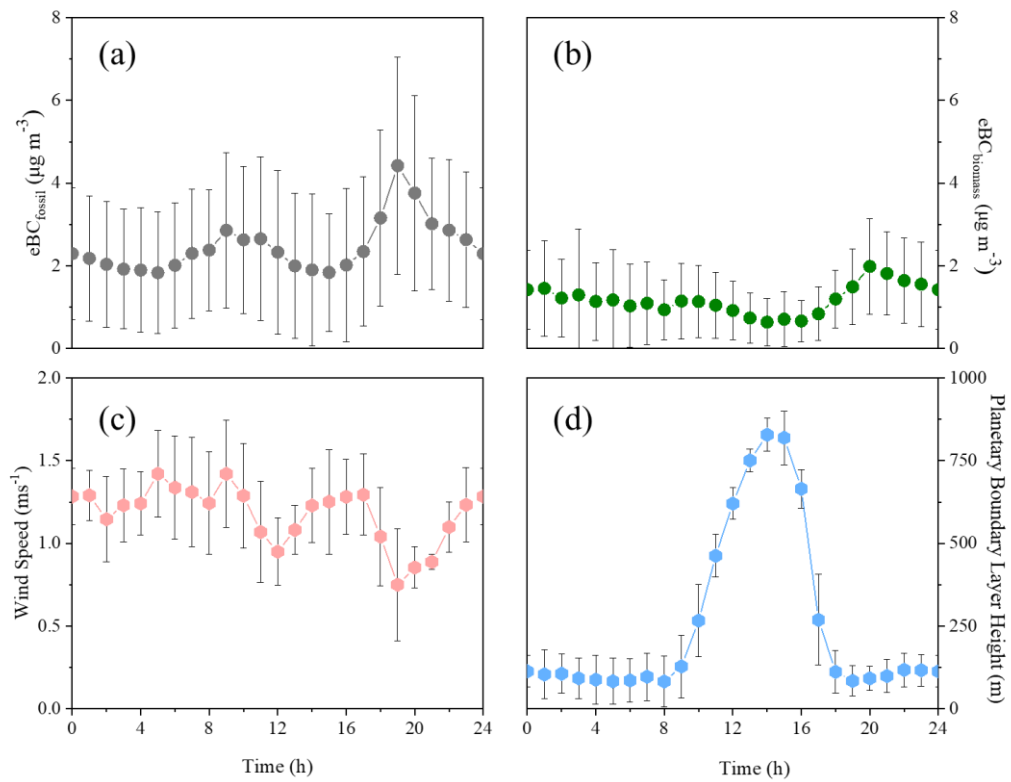
829 **Figure 5.** Direct radiative effect (DRE) of the eBC from fossil fuel combustion ($\text{eBC}_{\text{fossil}}$) shaded in grey and the eBC from
830 biomass burning ($\text{eBC}_{\text{biomass}}$) shaded in yellow (a) in the top atmosphere (TOA), surface (SUF), and the atmosphere atmospheric
831 column (ATM) and (b) the $\text{DRE}_{\text{eBC,ATM}}$ of two types of eBC under local scale dominance (LD) shaded in light grey labeled as
832 LD, local scale strong and regional scale weak (LSRW) shaded in light blue labeled as LSRW, local scale weak regional scale
833 strong (LWRS) shaded in light grey labeled with LWRS and regional scale dominance (RD) shaded in light blue labeled as RD
834 (c) DRE efficiencies of $\text{eBC}_{\text{biomass}}$ (shaded in yellow) and $\text{eBC}_{\text{fossil}}$ (shaded by grey) in TOA, SUF and ATM (d) DRE efficiencies
835 of $\text{eBC}_{\text{biomass}}$ and $\text{eBC}_{\text{fossil}}$ at ATM under LD (shaded in light grey labeled as LD), LSRW (shaded in light blue labeled as
836 LSRW), LWRS (shaded in light grey labeled as LWRS) and RD (shaded in light blue labeled with RD).

837 .



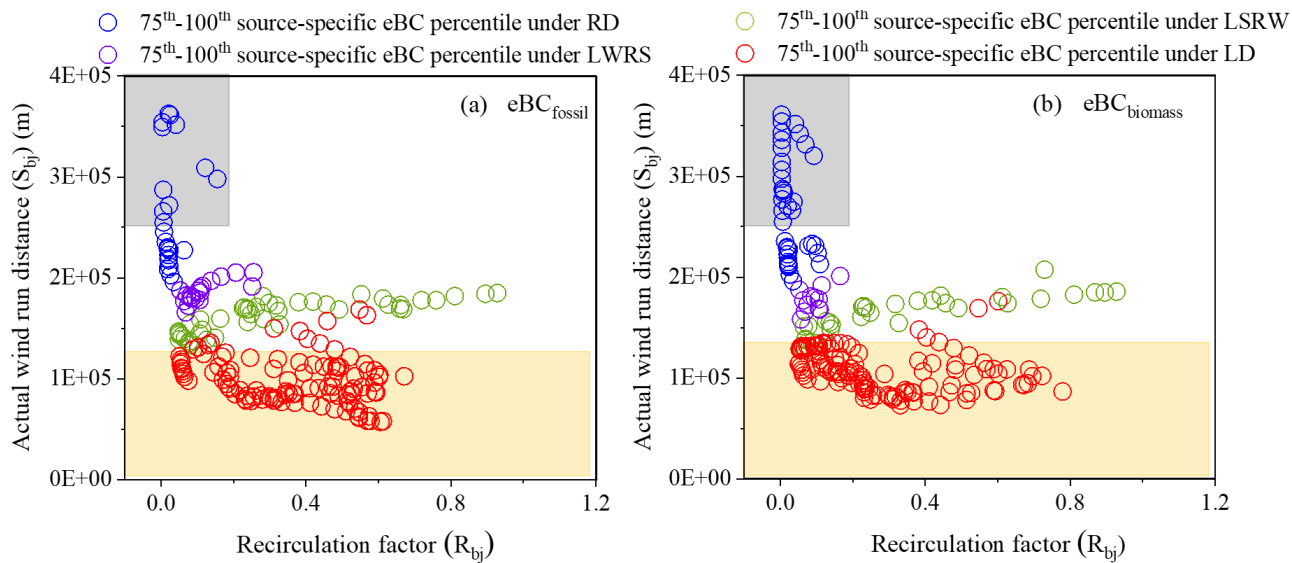
838

839 **Figure 1.** Four factors identified by source apportionment. Concentration ($\mu\text{g m}^{-3}$) of the chemical species and primary
 840 absorption coefficients (p_{abs}) (λ) at six wavelengths ($\lambda = 370, 470, 520, 590, 660, \text{ or } 880\text{nm}$) (M m^{-1}) for each source are shown
 841 in grey. The blue square represents the contribution of each chemical species to the four different factors.



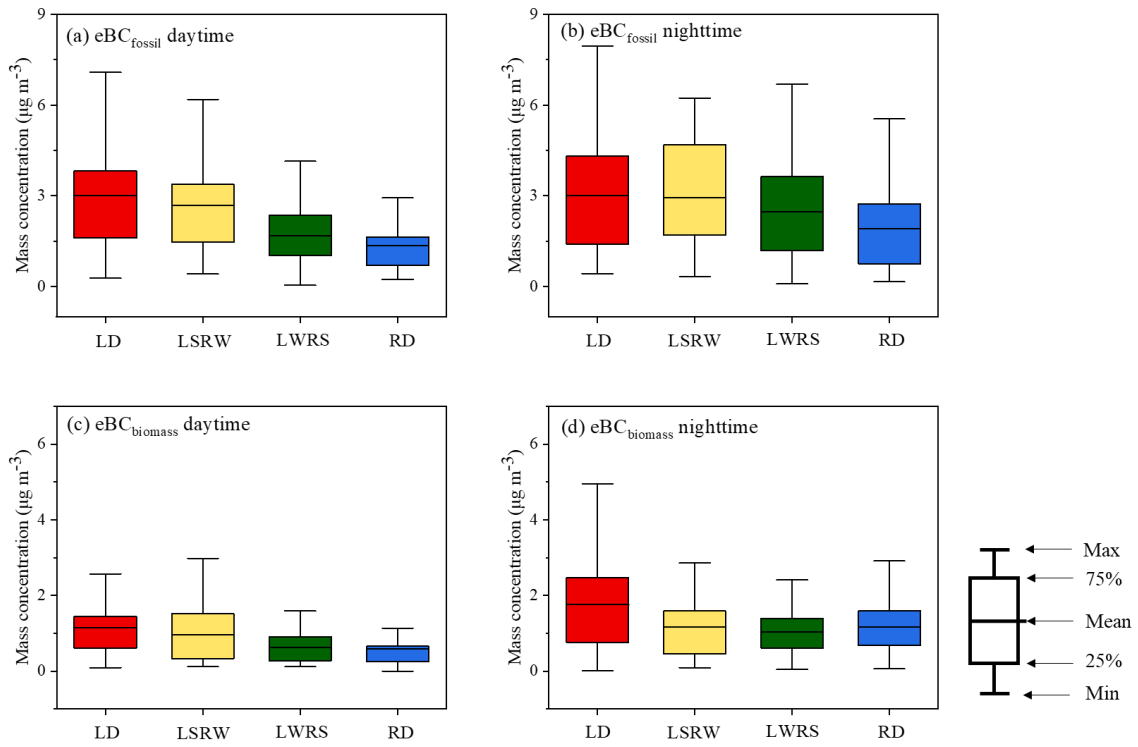
842

843 **Figure 2.** (a) Diel variations of the eBC from fossil fuel combustion (eBC_{fossil}) and (b) the eBC from biomass burning
 844 (eBC_{biomass}), (c) wind speed (m s⁻¹) and (d) planetary boundary layer height (m). The black bars of each hourly-averaged point
 845 show the standard deviation.



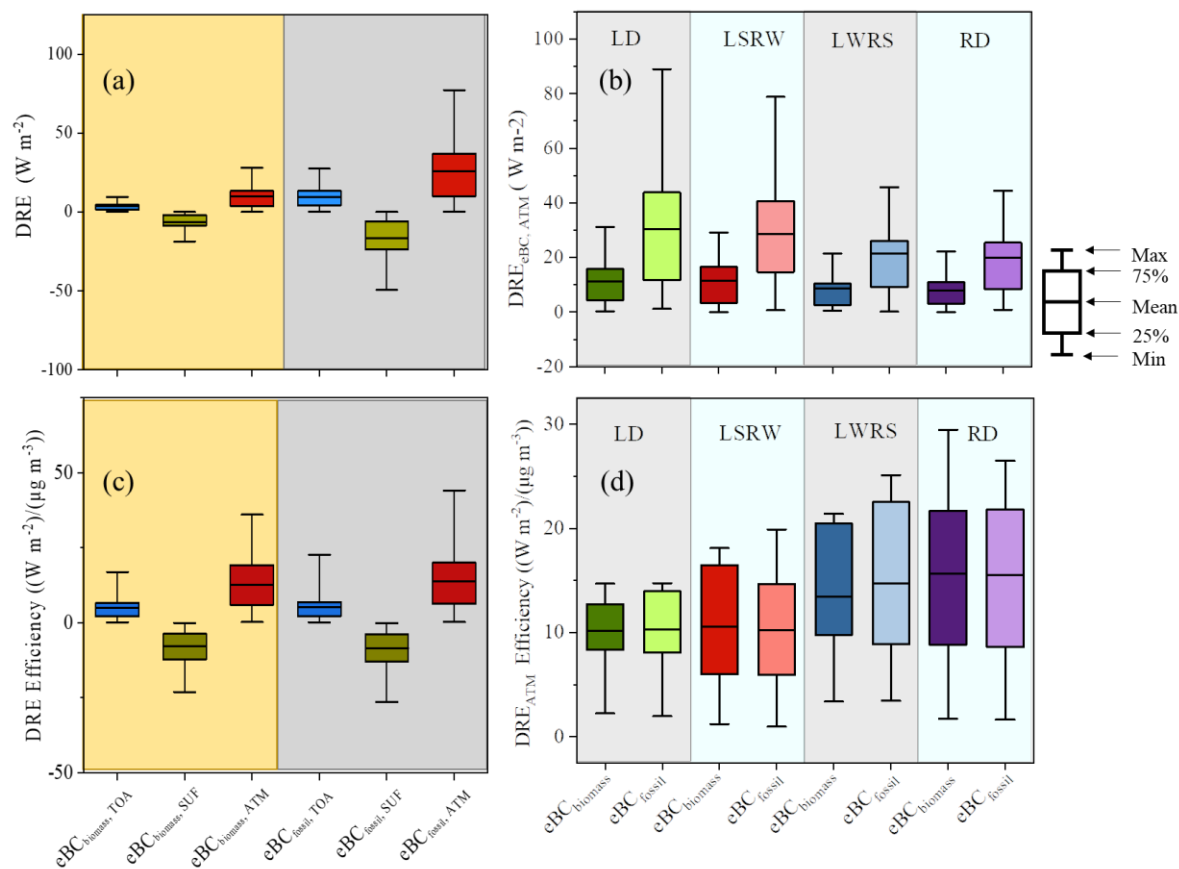
846

847 **Figure 3.** (a) The 75th – 100th percentile mass concentrations of the eBC from fossil fuel combustion (eBC_{fossil}) and (b) the eBC
 848 from biomass burning ($eBC_{biomass}$) under local scale dominance (LD, red circle), local scale strong and regional scale weak
 849 (LSRW, green circle), local scale weak regional scale strong (LWRS, purple circle) and regional scale dominance (RD, blue
 850 circle). S_{bj} is actual wind run distance at 100m height, R_{bj} is the recirculation factor, the grey area indicates good ventilation
 851 ($S_{bj} \geq 250\text{km}$, $R_{bj} \leq 0.2$), the yellow area indicates air stagnation ($S_{bj} \leq 130\text{km}$).



852

853 **Figure 4.** Mass concentrations of the eBC from fossil fuel combustion ($\text{eBC}_{\text{fossil}}$) and the eBC from biomass burning ($\text{eBC}_{\text{biomass}}$)
 854 during daytime (a, c) and nighttime (b, d) under local scale dominance (LD); local scale strong and regional scale weak
 855 (LSRW); local scale weak regional strong (LWRS); and regional scale dominance (RD).



857

858 **Figure 5.** Direct radiative effect (DRE) of the eBC from fossil fuel combustion (eBC_{fossil}) shaded in grey and the eBC from
 859 biomass burning ($eBC_{biomass}$) shaded in yellow (a) in the top atmosphere (TOA), surface (SUF), and the atmosphere atmospheric
 860 column (ATM) and (b) the $DRE_{eBC, ATM}$ of two types of eBC under local scale dominance (LD) shaded in light grey labeled as
 861 LD, local scale strong and regional scale weak (LSRW) shaded in light blue labeled as LSRW, local scale weak regional scale
 862 strong (LWRS) shaded in light grey labeled with LWRS and regional scale dominance (RD) shaded in light blue labeled as RD
 863 (c) DRE efficiencies of $eBC_{biomass}$ (shaded in yellow) and eBC_{fossil} (shaded by grey) in TOA, SUF and ATM (d) DRE efficiencies
 864 of $eBC_{biomass}$ and eBC_{fossil} at ATM under LD (shaded in light grey labeled as LD), LSRW (shaded in light blue labeled as
 865 LSRW), LWRS (shaded in light grey labeled as LWRS) and RD (shaded in light blue labeled with RD).

866